

RESEARCH ARTICLE SUMMARY

RECEPTORS

Structural basis for sugar perception by *Drosophila* gustatory receptors

Demin Ma[†], Meiqin Hu[†], Xiaotong Yang[†], Qiang Liu[†], Fan Ye, Weijie Cai, Yong Wang, Ximing Xu, Shenghai Chang, Ruiying Wang, Wei Yang, Sheng Ye, Nannan Su^{*}, Minrui Fan^{*}, Haoxing Xu^{*}, Jiangtao Guo^{*}

INTRODUCTION: Taste perception plays an essential role for animals to seek nutritious foods but avoid harmful compounds. Unlike mammals that detect sweet, umami, and bitter tastants via G protein-coupled receptors, insects harness a large group of ligand-gated ion channels called gustatory receptors (GRs) for the perception of sweet, bitter, and other tastes. Despite extensive physiological and genetic studies, how GRs recognize tastant molecules and transit from a closed state to an open conformation has remained unclear owing to the lack of three-dimensional structural information.

RATIONALE: Focusing on insect sweet taste receptors, we used cryo-electron microscopy to determine high-resolution structures of two clades of *Drosophila* sugar receptors, GR43a and GR64a, in both apo and sugar-bound states. We also performed electrophysiological and Ca²⁺ imaging assays to validate the structural findings.

RESULTS: When expressed in heterologous expression systems, GR43a and GR64a form sugar-gated cation channels that are specifically activated by a monosaccharide (fructose) and

disaccharides (sucrose and maltose), respectively. Structures of GR43a and GR64a at 2.5- to 2.6-Å resolutions revealed that GRs are tetrameric ion channels. Each GR subunit contains seven transmembrane helices (S1 to S7) with S1 to S6 forming the ligand-binding domain (LBD) and S7 contributing to the formation of the central pore domain (PD). In the apo state, the channel pores of both GRs are closed. At the cytosolic side of the GR channel, four lateral conduits between adjacent subunits act as potential ion exit routes.

Structures of GR43a and GR64a in the sugar-bound states revealed that sugars bind to the extracellular-facing pockets of LBDs through hydrogen bonds and CH- π interactions. GR43a recognizes fructose with a narrow pocket that can neither accommodate disaccharides nor optimally fit other monosaccharides, such as glucose. Mutating the fructose-interacting residues severely impaired the channel activity of GR43a. GR64a binds disaccharides with a larger and flatter pocket that has the structural plasticity to accommodate both sucrose and maltose but not monosaccharides. Overall, the sugar-binding pocket of GR is shallow and polar, suitable for recognizing nonvolatile, water-soluble tastant compounds.

In the sugar-bound structures of GR43a and GR64a, the channel pores remain closed. To understand how sugar binding triggers the opening of the channel pore, we identified a GR43a mutant (GR43a-I418A), which showed constitutive activity and can be further activated by fructose. Using this GR43a mutant in the presence of fructose, we determined the structure of GR43a in an open conformation, in which the channel pore is dilated and large enough for cation permeation. By comparing structures of GR43a in the apo closed, fructose-bound closed, and fructose-bound open conformations, we uncovered the fructose activation mechanism of GR43a. The binding of fructose to the LBDs induces motions of S5 and S6 toward the ligand-binding pocket center, which then causes a bending of pore-lining S7 to open the channel pore through hydrogen bonds and hydrophobic interactions between S5 and S7.

CONCLUSION: Our work reveals how sugar molecules bind to activate insect sweet taste receptors, providing a prototypical platform for understanding how different tastants are perceived by diverse members of the insect GR family. Because taste perception plays an important role in the regulation of insect physiology and behavior, this study also offers accurate structural models for the rational design of attractant or repellent modulators for pest control. ■

The list of author affiliations is available in the full article online.

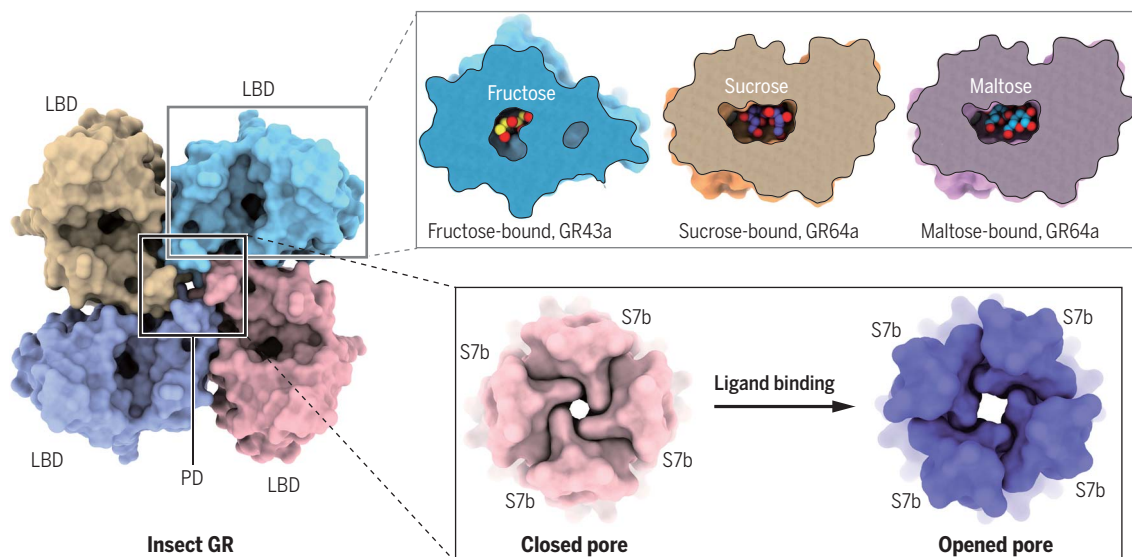
*Corresponding author. Email: jiangtaoquo@zju.edu.cn (J.G.); haoxingx@zju.edu.cn (H.X.); mrfan@cemps.ac.cn (M.F.); sunnannan@zju.edu.cn (N.S.)

[†]These authors contributed equally to this work.

Cite this article as D. Ma et al., *Science* **383**, eadj2609 (2024). DOI: 10.1126/science.adj2609

S READ THE FULL ARTICLE AT
https://doi.org/10.1126/science.adj2609

Molecular basis for sugar perception by insect GRs. Insect GRs are tetrameric cation channels with four peripheral LBDs and one central PD. Sugar molecules bind to LBDs to trigger conformational changes, which are then transferred to the PD to induce the opening of the channel pore.



RESEARCH ARTICLE

RECEPTORS

Structural basis for sugar perception by *Drosophila* gustatory receptors

Demin Ma^{1,2,†}, Meiqin Hu^{3,4,†}, Xiaotong Yang^{3,4,†}, Qiang Liu^{3,4,†}, Fan Ye^{1,2}, Weijie Cai^{3,4}, Yong Wang⁵, Ximing Xu⁶, Shenghai Chang⁷, Ruiying Wang⁸, Wei Yang^{1,9}, Sheng Ye¹⁰, Nannan Su^{11*}, Minrui Fan^{8*}, Haoxing Xu^{3,4,12*}, Jiangtao Guo^{1,2,9,13,14,15*}

Insects rely on a family of seven transmembrane proteins called gustatory receptors (GRs) to encode different taste modalities, such as sweet and bitter. We report structures of *Drosophila* sweet taste receptors GR43a and GR64a in the apo and sugar-bound states. Both GRs form tetrameric sugar-gated cation channels composed of one central pore domain (PD) and four peripheral ligand-binding domains (LBDs). Whereas GR43a is specifically activated by the monosaccharide fructose that binds to a narrow pocket in LBDs, disaccharides sucrose and maltose selectively activate GR64a by binding to a larger and flatter pocket in LBDs. Sugar binding to LBDs induces local conformational changes, which are subsequently transferred to the PD to cause channel opening. Our studies reveal a structural basis for sugar recognition and activation of GRs.

Animals use the taste sensory system to detect nutritive food ingredients and to avoid toxic compounds. Humans have five taste sensations—namely sweet, bitter, salty, sour, and umami (1–3). In insects such as *Drosophila*, various tastants can also induce taste sensations of sweet, bitter, salty, and sour (3–5). In *Drosophila*, taste perception is initiated by the recognition of tastant molecules by specific receptors expressed in gustatory receptor neurons, which are located on external taste organs, such as the anterior wing margins, legs, and labellum, as well as on three internal taste organs inside the proboscis (5–7). Among different taste receptor proteins in *Drosophila*, the gustatory receptors (GRs) play a major role in the sensation of sweet, bitter, and other tastes (5, 7–9).

The *Drosophila* GR family, which is distantly related to the olfactory receptor (OR) family, comprises 68 members that all share a seven-transmembrane (7TM)-helical domain and a relatively conserved C-terminal motif (10–13). GRs are proposed to function as ligand-gated ion channels, representing one of the largest ion channel families (14–16). GRs confer sensations of diverse chemical and physical stimuli, such as sweet (17–27) and bitter (28–32) tastants,

CO₂ (33, 34), pheromones (30, 35, 36), temperature (37), light (38, 39), and repellents (40–42). Among these, sweet sensation is particularly important because of its role in detecting sugars and regulating carbohydrate intake (43–45). Sweet taste sensation is primarily mediated by nine GRs, including GR5a, GR43a, GR61a, and GR64a to GR64f (17–27). GR5a, GR61a, and GR64a to GR64f belong to a clade of sweet taste receptors that are required for sensing multiple sugars in peripheral gustatory receptor neurons (13, 17–22, 25–27). As a conserved fructose-specific receptor in another GR clade, GR43a functions as a nutrient sensor in the *Drosophila* brain and plays a critical role in controlling feeding behavior (23, 24). Additionally, GR43a is the major sugar receptor in *Drosophila* larvae (23, 24, 46). Of these sugar receptors, GR64a mediates the perception of not only natural sugars but also the artificial sweetener sucralose (47).

Although the genetics and in vivo physiology of *Drosophila* sweet taste receptors have been extensively studied (17–27), the underlying molecular mechanisms remain largely unknown. For example, the sugar selectivity of these sweet taste receptors needs to be clarified in vitro. In addition, the structural basis for sugar percep-

tion by different GRs awaits experimental investigation. In this study, we performed functional, structural, and structure-guided mutational studies of the *Drosophila melanogaster* sweet taste receptors GR43a and GR64a. By determining cryo-electron microscopy (cryo-EM) structures of both GRs in their apo and sugar-bound states, we revealed the structural and functional mechanisms by which monosaccharides and disaccharides can selectively bind to and activate distinct GRs.

GR43a and GR64a are sugar-activated cation channels

To functionally characterize *Drosophila* sweet taste receptors, we heterologously expressed GR43a and GR64a in human embryonic kidney 293FT (HEK293FT) cell lines and measured whole-cell currents in the otherwise sugar-free recording solutions with or without bath perfusion of various sugars—fructose, glucose, maltose, and sucrose (Fig. 1 and figs. S1 and S2). Non-transfected HEK293FT cells lacked any measurable response to sugar application (Fig. 1, A and B). By contrast, in the GR43a-transfected HEK293FT cells, fructose—but not glucose, maltose, or sucrose—evoked large whole-cell currents (Fig. 1, C and D). Ion substitution experiments indicate that the fructose-evoked GR43a-dependent currents (I_{GR43a}) are mediated by cations but not anions in the recording solutions. Based on the reversal potential (E_{rev}) measurement under bi-ionic conditions, GR43a was found to be permeable to Na⁺, K⁺, Ca²⁺, and Cs⁺ with a poor selectivity among them (fig. S1B). To exclude any contamination with endogenous K⁺ and Cl[−] channels, we used a Cl[−]-free Cs⁺-based pipette (cytosolic) solution (Materials and methods) in further studies. Fructose robustly activated I_{GR43a} in a dose-dependent manner with a half maximal effective concentration (EC₅₀) of 10.7 ± 2.1 mM (Fig. 1, E and F). To reveal the maximal activation with the full concentration range of sugars, we used an ion-free extracellular solution with mannitol supplementation for osmolarity adjustment (Materials and methods). Similar electrophysiological results were seen in Chinese Hamster Ovary (CHO) and COS1 monkey cell lines when they were transfected with GR43a (fig. S1, G and H). Consistently, in the Ca²⁺ imaging assays, fructose, but not glucose or disaccharide, induced GR43a-specific Ca²⁺

¹Department of Biophysics and Department of Neurology of the Fourth Affiliated Hospital, Zhejiang University School of Medicine, Hangzhou, Zhejiang 310058, China. ²Nanhu Brain-Computer Interface Institute, Hangzhou 311100, China. ³Department of Neurology and Department of Cardiology, The Second Affiliated Hospital of Zhejiang University School of Medicine, Hangzhou 310058, China. ⁴New Cornerstone Science Laboratory, Liangzhu Laboratory and School of Basic Medical Sciences, Zhejiang University, Hangzhou 311121, China. ⁵College of Life Sciences, Zhejiang University, Hangzhou, Zhejiang 310058, China. ⁶Marine Biomedical Institute of Qingdao, School of Pharmacy and Medicine, Ocean University of China, Qingdao, Shandong 266100, China. ⁷Center of Cryo-Electron Microscopy, Zhejiang University School of Medicine, Hangzhou 310058, China. ⁸CAS Center for Excellence in Molecular Plant Sciences, Institute of Plant Physiology and Ecology, Chinese Academy of Sciences, Shanghai 200032, China. ⁹NHC and CAMS Key Laboratory of Medical Neurobiology, MOE Frontier Science Center for Brain Science and Brain-machine Integration, School of Brain Science and Brain Medicine, Zhejiang University, Hangzhou, Zhejiang 310058, China. ¹⁰Tianjin Key Laboratory of Function and Application of Biological Macromolecular Structures, School of Life Sciences, Tianjin University, Tianjin 300072, China. ¹¹International Institutes of Medicine, The Fourth Affiliated Hospital, Zhejiang University School of Medicine, Yiwu, Zhejiang 322000, China. ¹²Department of Molecular, Cellular, and Developmental Biology, University of Michigan, Ann Arbor, MI 48109, USA. ¹³State Key Laboratory of Plant Environmental Resilience, College of Life Sciences, Zhejiang University, Hangzhou 310058, China. ¹⁴Department of Cardiology, Key Laboratory of Cardiovascular Intervention and Regenerative Medicine of Zhejiang Province, Sir Run Run Shaw Hospital, Zhejiang University School of Medicine, Hangzhou, Zhejiang 310016, China. ¹⁵Cancer Center, Zhejiang University, Hangzhou, Zhejiang 310058, China.

*Corresponding author. Email: jiangtaoguo@zju.edu.cn (J.G.); haoxingx@zju.edu.cn (H.X.); mrfan@cemps.ac.cn (M.F.); sunannan@zju.edu.cn (N.S.)

†These authors contributed equally to this work.

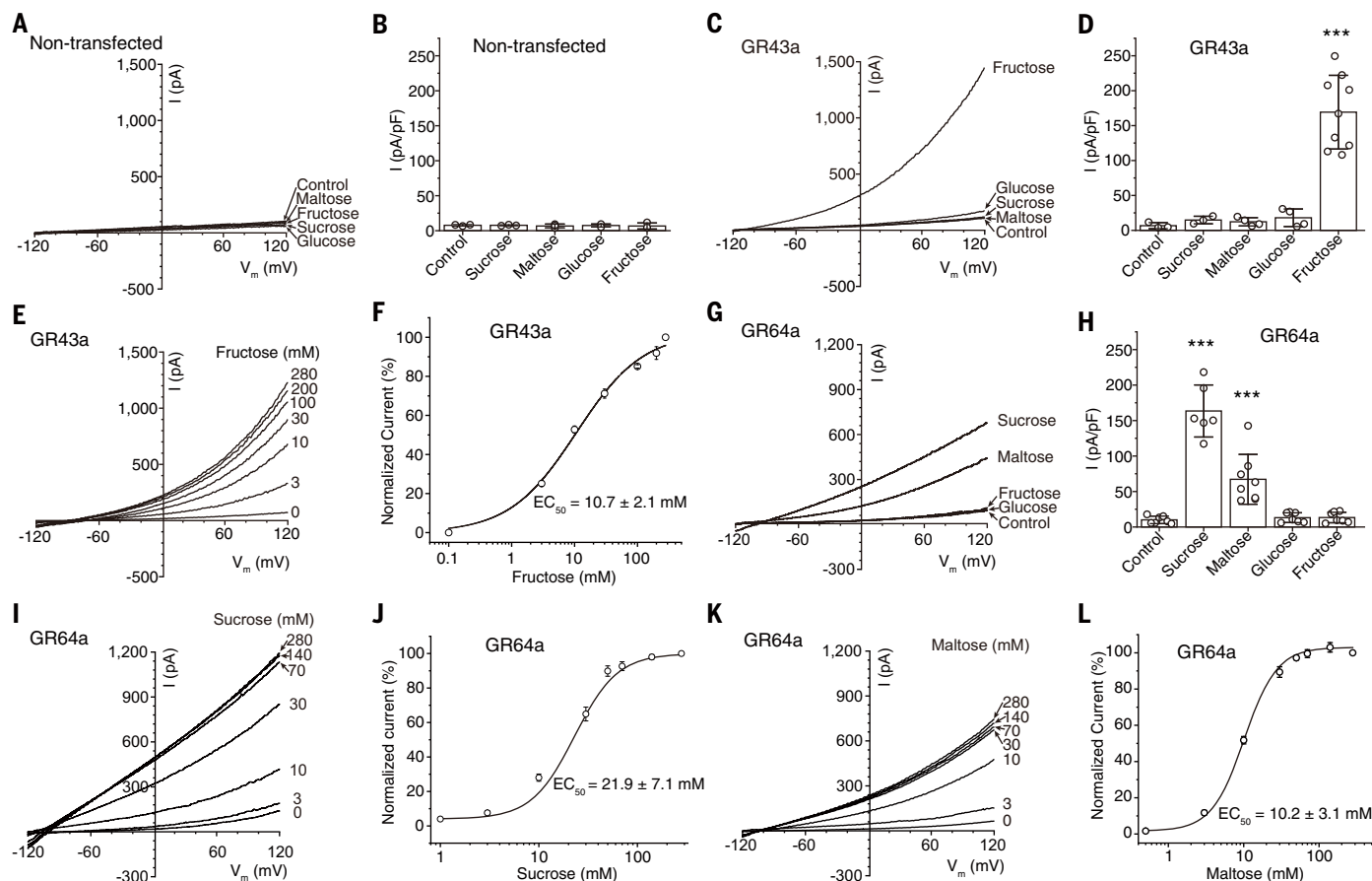


Fig. 1. Electrophysiological characterization of GR43a and GR64a.

(A) Whole-cell currents recorded in nontransfected HEK293FT cells treated with or without different sugars. (B) Summary of current density (pA/pF, measured at +120 mV) from experiments shown in (A). $n = 3$ independent experiments. (C) Whole-cell currents in GR43a-expressing HEK293FT cells treated with or without different sugars. (D) Summary of current density (pA/pF, measured at +120 mV) from experiments shown in (C). $n = 3, 3, 4, 4$, and 9 independent experiments. (E) Whole-cell currents in GR43a-expressing HEK293FT cells treated with fructose in different concentrations. (F) Concentration-dependent fructose activation of GR43a. All currents were normalized to that at +120 mV in the presence of 280 mM fructose shown in (E). $n = 3$ independent experiments. (G) Whole-cell currents recorded in GR64a-expressing HEK293FT cells treated

with or without different sugars. (H) Summary of current density (pA/pF, measured at +120 mV) from experiments shown in (G). $n = 7, 6, 8, 7$, and 7 independent experiments. (I) Whole-cell currents in GR64a-expressing HEK293FT cells treated with sucrose in different concentrations. (J) Concentration-dependent sucrose activation of GR64a. Currents were normalized to that at +120 mV in the presence of 280 mM sucrose shown in (I). $n = 5$ independent experiments. (K) Whole-cell currents in GR64a-expressing HEK293FT cells treated with maltose in different concentrations. (L) Concentration-dependent maltose activation of GR64a. Currents were normalized to that at +120 mV in 280 mM maltose shown in (K). $n = 5$ independent experiments. In (D) and (H), data are presented as means \pm SDs; statistical analyses were performed using two-tailed Student's t test to compare cell current density evoked with each sugar and without sugar (control). *** $P < 0.001$.

responses (fig. S3, A and B). Taken together, these results suggest that GR43a forms a fructose-activated, Ca^{2+} -permeable nonselective cation channel and that GR43a displays a strong ligand preference to fructose over glucose or disaccharide. Our conclusions agree with previous *in vivo* Ca^{2+} imaging studies (23) as well as with electrophysiological studies on both GR43a and its ortholog BmGR-9 from silkworm *Bombyx mori* (16).

We also investigated the sugar activation effects on GR64a and demonstrated that GR64a itself is also able to form a sugar-activated non-selective cation channel in our experimental paradigms (Fig. 1, G to L, and fig. S2, B, D, and E). However, in both electrophysiological and Ca^{2+} imaging assays, GR64a is activated by maltose

and sucrose—two disaccharides found in the fly food—but not by monosaccharide fructose or glucose (Fig. 1, G and H, and fig. S3, E and F). The disaccharide sensitivity of GR64a is generally consistent with previous electrophysiological studies of gustatory receptor neurons in *Drosophila* (19) as well as the two-way choice behavioral assays (20). Collectively, our results revealed that GR43a and GR64a are ionotropic sugar receptors with distinct sugar selectivity.

Overall structures of GR43a and GR64a

To uncover the sugar activation mechanisms of insect GRs, we determined cryo-EM structures of wild-type (WT) GR43a and GR64a in the apo (GR43a_{apo} and GR64a_{apo}) and sugar-bound states (GR43a_{fructose}, GR64a_{sucrose}, and GR64a_{maltose}) at

2.5- to 2.6-Å resolutions (Fig. 2, A to E, and figs. S4 to S7). All five maps are of high quality in most regions, which allowed us to accurately model 89% of both GR43a and GR64a proteins in the structures (figs. S5 and S7). GR43a_{apo} and GR64a_{apo} share similar overall architectures and domain organizations, with a root mean square deviation (RMSD) of 2.7 Å over 381 Ca atoms within one subunit when they are aligned (Fig. 2, A and C, and fig. S8). Hereafter, we use the GR43a_{apo} structure for analyzing the overall structure of GRs unless otherwise mentioned.

The GR43a channel is a tetramer composed of four symmetric subunits with dimensions of 82 Å by 82 Å by 90 Å (Fig. 2A and fig. S9), consistent with recent cross-linking and single-

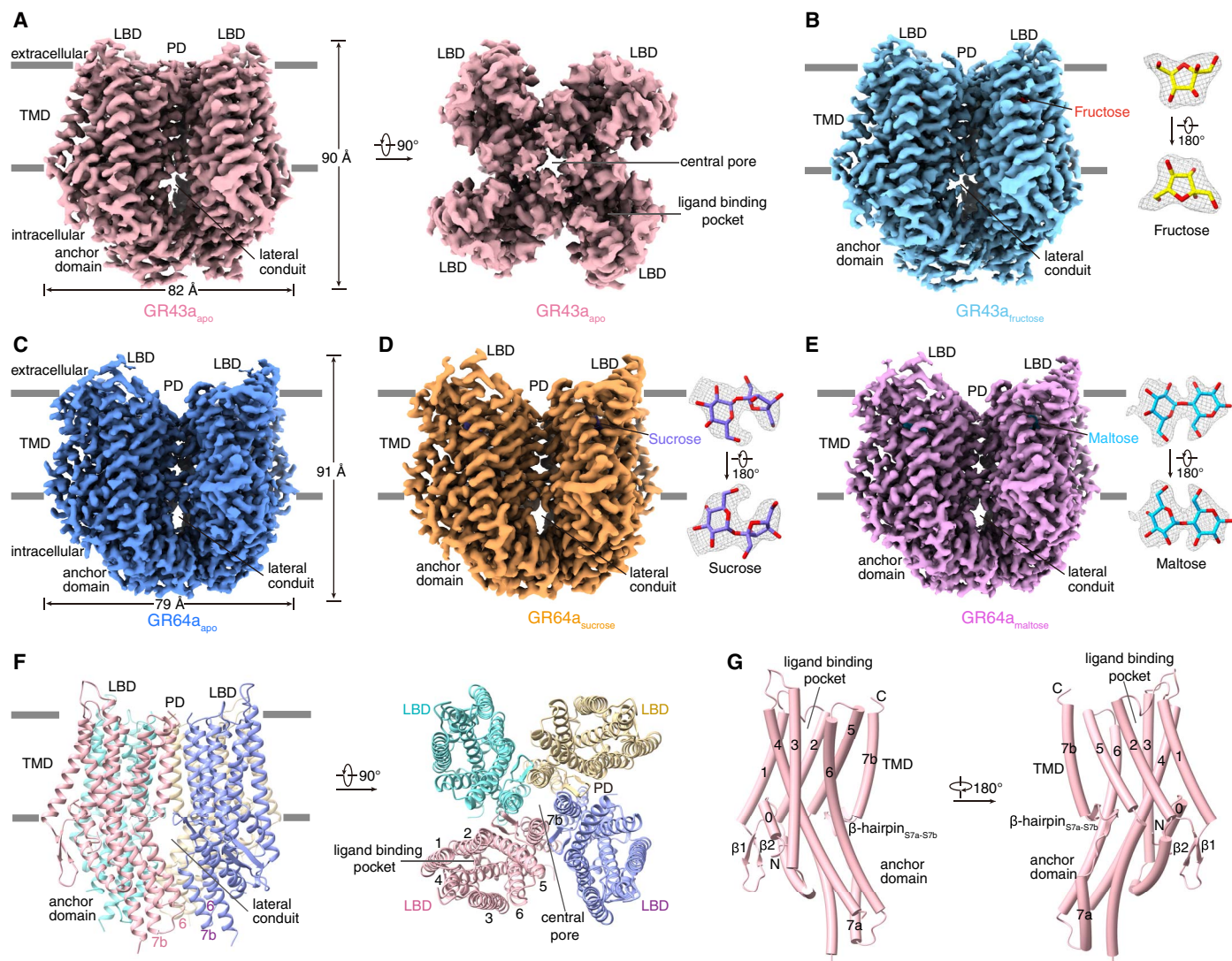


Fig. 2. Structures of GR43a and GR64a. (A) 3D reconstruction of GR43a_{apo} in side and top views. (B) 3D reconstruction of GR43a_{fructose} in side view. The fructose density is shown at the contour level of 5.8 σ . (C–E) 3D reconstructions of GR64a_{apo} (C), GR64a_{sucrose} (D), and GR64a_{maltose} (E) in side view. Densities of sucrose and maltose are shown at the contour levels of 4.2 σ and 4.8 σ , respectively. (F) Cartoon model of GR43a_{apo} in side and top views. Each subunit is colored individually. (G) Side view of one GR43a_{apo} subunit. The numbers indicate transmembrane segments S1 to S7.

molecule imaging studies of the GR43a ortholog BmGR-9 (48). Each subunit contains seven transmembrane helices (S1 to S7), with the N terminus facing the cytosolic side and the C terminus facing the extracellular side (Fig. 2, F and G), opposite to the topological organization of the 7TM G protein-coupled receptors (49). The long S7 helix breaks into two parts: the S7a in the cytosolic portion, and the S7b in the transmembrane domain (TMD) (Fig. 2G). Four S7b helices each from one subunit form the putative ion-conducting pore domain (PD) in the center (Fig. 2F). In the periphery, helices S1 to S6 from each subunit assemble into the ligand-binding domain (LBD) with an extracellular-facing pocket that can accommodate sugar molecules (Fig. 2F), as shown in the sugar-bound structures. The PD and LBD are mainly coupled

by intrasubunit interactions between S7 and S5-S6 (Fig. 2F). The extensions of S4, S5, S6, and S7 (S7a) form a cytosolic anchor domain (Fig. 2G) that is involved in the channel's tetrameric assembly through intersubunit interactions of S6 and S7b (Fig. 2F). By contrast, there are only short loops on the extracellular side (Fig. 2, F and G). Despite low sequence identity (12%), the overall structure of GR43a resembles a previously reported structure of the OR MhOR5 from the jumping bristletail *Machilis hrabei* (50), with an RMSD of 2.8 Å over 377 C α atoms within one subunit when they are aligned (fig. S10A).

The closed ion-conducting pore in GR43a

Along the central axis of GRs, a putative ion-conducting pathway spans both the TMD and

the anchor domain (Fig. 3A). In the TMD of GR43a_{apo}, four S7b helices constitute a funnel-shaped pore, which opens to the cytosolic side and closes near the extracellular surface of the membrane (Fig. 3A). The extracellular gate is closed by constrictions formed by hydrophobic residues Ile⁴¹⁸ and Phe⁴²², with a pore radius below 1 Å (Fig. 3A). On the inner surface of the central pore, there are multiple polar residues, including Thr⁴⁰³, Ser⁴⁰⁷, Ser⁴¹⁰, and Thr⁴¹⁴, which may favor the passage of the hydrated ions (Fig. 3A). The major part of the S7a-S7b linker (Phe³⁹²-Arg³⁹⁹) folds into a short β -hairpin (β -hairpin_{S7a-S7b}) on the cytosolic surface of the membrane that participates in building up the central pore through the intersubunit hydrogen bonds Cys³⁹⁵-Arg⁴⁰² and Leu³⁹⁷-Thr⁴⁰⁶ and a hydrophobic interaction Leu³⁹⁷-Leu⁴⁰⁵,

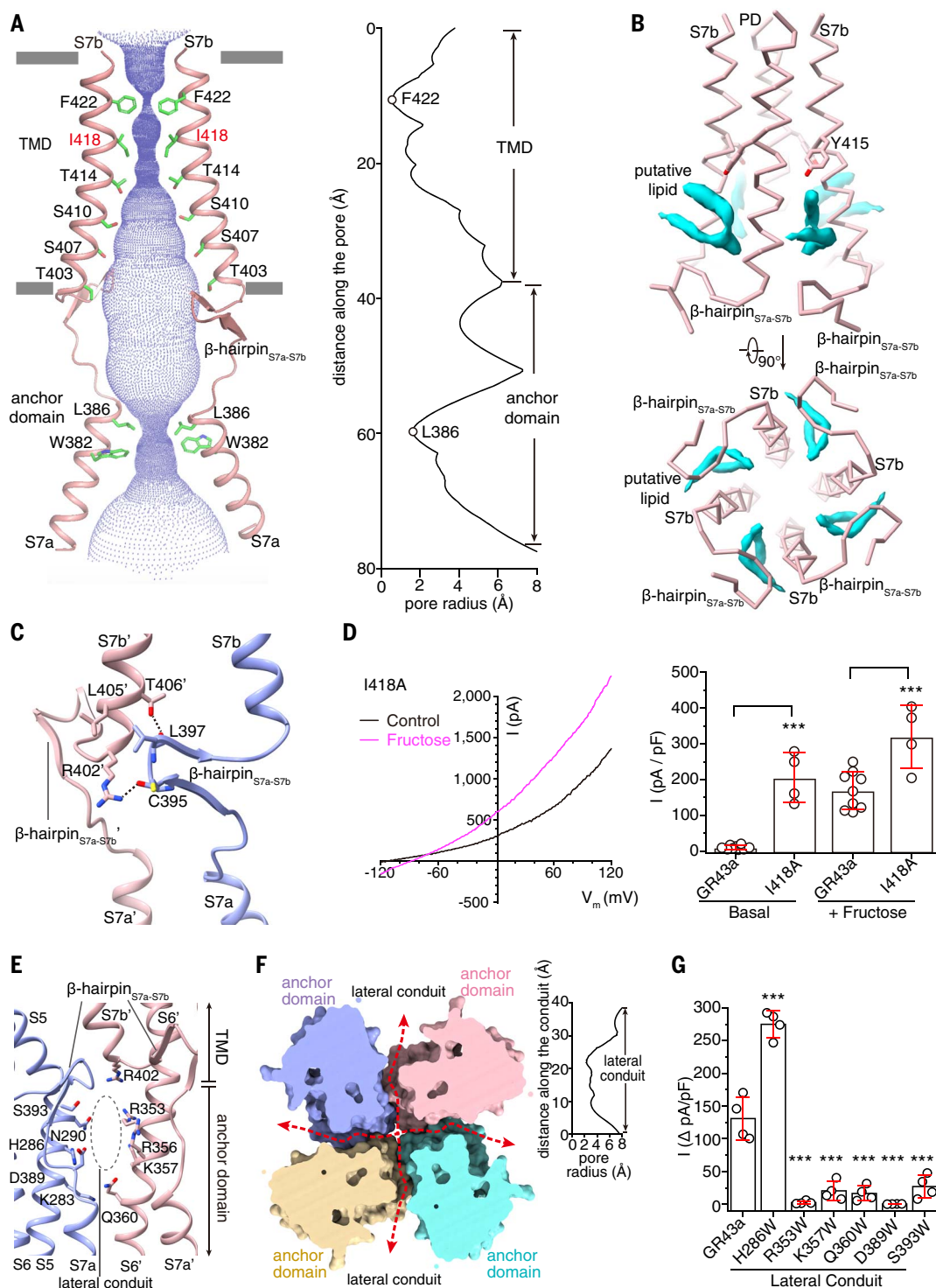


Fig. 3. The ion-conducting pore of GR43a. (A) The central pore of GR43a with front and rear subunits removed for clarity (left) and pore radius along the central axis calculated using the HOLE program (right). The central pathway is marked with a dotted mesh. (B) β -hairpin_{S7a-S7b} and putative lipids (cyan densities) participate in building up the central pore. (C) β -hairpin_{S7a-S7b} mediates intersubunit interactions. Hydrogen bonds are marked with dashed lines. (D) Whole-cell currents in HEK293FT cells transfected with the I418A mutant of GR43a treated with or without fructose (left) and summary of current density (pA/pF, measured at +120 mV) in comparison with the wild type (right). $n = 9$ and 4 independent experiments. Data are presented as means \pm SDs.

Two-tailed Student's t test was performed to compare current density of cells expressing WT and mutant GR43a evoked without fructose (basal) or with fructose. *** $P < 0.001$. (E) Hydrophilic residues located on the surface of the lateral conduit. (F) The four lateral conduits between adjacent subunits in the cytosolic region shown in the surface model in the cut-in top view (left) and the pore radius along the lateral conduit calculated using the HOLE program (right). The red dashed arrows indicate ion permeation pathways along the lateral conduits. (G) Density of fructose-evoked whole-cell currents ($\Delta pA/pF$, measured at +120 mV) in HEK293FT cells that were transfected with WT or mutant GR43a. $n = 4, 4, 4, 4, 4, 4$, and 4 independent experiments. The six mutated

amino acid residues are located on the surface of the lateral conduit, as shown in (E). Data are presented as means \pm SDs. Two-tailed Student's *t* test was performed to compare the current density of cells expressing WT GR43a and each

mutant. ****P* < 0.001. Single-letter abbreviations for the amino acid residues are as follows: A, Ala; C, Cys; D, Asp; E, Glu; F, Phe; G, Gly; H, His; I, Ile; K, Lys; L, Leu; M, Met; N, Asn; P, Pro; Q, Gln; R, Arg; S, Ser; T, Thr; V, Val; W, Trp; and Y, Tyr.

(Fig. 3, A to C). Above the β -hairpin_{S7a-S7b} and underneath a conserved tyrosine residue (Tyr⁴¹⁵) in S7b (10, 11, 51), a lipid-shaped density is observed between two adjacent S7b helices (Fig. 3B). This putative lipid, whose hydrophilic head points to the pore center, also contributes to the formation of the central pore by sealing the lateral fenestration with its hydrophobic tails (Fig. 3B), as revealed by molecular dynamics (MD) simulations. Without this putative lipid, water molecules in the central pore cavity of GR43a might “leak” into the surrounding membranes through lateral fenestrations, as seen in the simulations (fig. S11). Spontaneous binding of lipids from the lipid bilayer to the cryo-EM-defined pockets was also observed, aligning well with the putative lipid densities observed in cryo-EM maps (fig. S11 and movie S1). Therefore, although the central pore of GRs is lined by only one helix S7b for each subunit, the presence of the β -hairpin_{S7a-S7b} and the putative lipid ensures the structural integrity of the central pore (Fig. 3B). To verify that ions pass through this central pore in the TMD, we mutated the constriction residues Phe⁴²² and Ile⁴¹⁸ both to alanine. Whereas the F422A (Phe⁴²² \rightarrow Ala⁴²²) mutation resulted in a non-functional channel that cannot be activated by fructose (fig. S1D), the I418A mutant became a constitutively active channel that can be further activated by fructose (Fig. 3D and fig. S1C). This activation gating effect of I418A supports the ion-conducting role of the central pore in the TMD.

Four anchor domains constitute the cytosolic central pore mainly through helix S7a (Fig. 3A). In GR43a_{apo}, this cytosolic central pore has two layers of constrictions formed by residues Leu³⁸⁶ and Trp³⁸², with a pore radius of ~ 1.7 Å (Fig. 3A). Between two adjacent subunits, a lateral conduit is formed by the cytosolic parts of S5 and S6', as well as the S7a-S7b linker (Fig. 2A and Fig. 3, E and F). This lateral conduit is mainly lined by hydrophilic residues, including Lys²⁸³, His²⁸⁶, and Asn²⁹⁰ in S5; Arg³⁵³, Arg³⁵⁶, Lys³⁵⁷, and Gln³⁶⁰ in S6'; and Asp³⁸⁹, Ser³⁹³, and Arg⁴⁰² in the S7a-S7b linker (Fig. 3E). With a van der Waals pore radius of at least ~ 2.5 Å throughout its length (Fig. 3F), the lateral conduit might be large enough for the permeation of partially hydrated Na⁺ and K⁺. To investigate whether this lateral conduit might mediate an ion conduction pathway, as demonstrated in the Piezo channel (52, 53), we mutated the conduit-lining hydrophilic amino acid residues into Trp, a bulky hydrophobic residue. Among the six Trp-substituted mutants, five displayed much-reduced current amplitudes

(Fig. 3G and fig. S1F), likely caused by a steric hinderance of the ion conduction pathway.

Structural basis for fructose recognition in GR43a

In the 2.5-Å-resolution map of GR43a_{fructose}, a strong fructose-shaped density was observed in the extracellular-facing pocket of the LBD (Fig. 2B and fig. S5D). Because no similar density is observed in this pocket of GR43a_{apo} (fig. S5B), we attributed this density to fructose. The high-resolution map allowed us to accurately model the fructose as a β -D-fructofuranose isomer (Fig. 2B), which accounts for $\sim 80\%$ of fructose in the fructose-protein complex structures in the Protein Data Bank (54). To further validate this fructose-binding mode, we ran all-atom MD simulations, which show that the fructose can stably bind in this pocket throughout 500 ns with an RMSD within 3 Å (fig. S12, A to C). The fructose sits in a narrow pocket mainly lined by S2 to S6 and the S1-S2 linker, forming extensive hydrogen bonds with surrounding residues, including Arg⁷⁰ in the S1-S2 linker, Asp⁸³ in S2, Asp¹⁵⁰ in S3, Tyr¹⁸² in S4, His³⁰⁶ and Thr³¹⁰ in S5, and His³³⁷ in S6 (Fig. 4, A and B). In addition, the furanose ring of fructose and the side chain of Trp³³³ in S6 form a CH- π interaction (Fig. 4B), a characteristic interaction between sugars and aromatic residues in sugar-binding proteins (55), such as the *Vibrio parahaemolyticus* sodium-galactose symporter (vSGLT) (56).

To verify the fructose-binding pocket, we introduced alanine substitution mutations at the eight abovementioned fructose-interacting residues in GR43a and studied fructose activation using electrophysiology in the HEK293FT cells expressing these mutant channels. Compared with WT GR43a, all mutants displayed abolished or reduced fructose-evoked currents (Fig. 4C and fig. S1E), which suggests that fructose in fact activates GR43a by binding to this pocket in the LBD. As negative controls, mutating residues Ser²¹², Asn²⁶⁶, and Leu²⁶⁹ that are located outside the fructose-binding pocket failed to affect fructose activation (Fig. 4C). Consistent results were seen when these mutant GR43a channels were analyzed using Ca²⁺ imaging assays (fig. S3, C and D). The eight fructose-interacting residues are conserved in other GR43a orthologs, such as BmGR-9 (fig. S13A). A previous study had reported that mutations on equivalent sites of BmGR-9 similarly abolished the activation of BmGR-9 by fructose (48). Therefore, the fructose-binding sites revealed in GR43a_{fructose} are supported and confirmed by functional studies.

Structural basis for sucrose and maltose recognition in GR64a

In the LBDs of GR64a_{sucrose} and GR64a_{maltose}, we also observed strong nonprotein densities that are not present in the LBD of GR64a_{apo} and modeled one sucrose molecule and one maltose molecule, respectively (Fig. 2, D and E; Fig. 4, D, E, G, and H; and fig. S7, B, D, and F). The binding poses of sucrose and maltose were further confirmed by MD simulations (fig. S12, D to I). Different from the narrow fructose-binding pocket in GR43a, the ligand-binding pocket in GR64a is larger and flatter (Fig. 4, D and G). It is lined by all six helices in the LBD, as well as the long S3-S4 linker, which contains two short helices (Fig. 4, E and H). Both sucrose and maltose are also mainly recognized by GR64a through multiple hydrogen bonds (Fig. 4, E and H). Moreover, the two disaccharides are sandwiched by side chains of aromatic residues Tyr²⁰⁰ in S3 and Phe¹³⁴ in S2, resulting in more CH- π interactions (Fig. 4, E and H).

To confirm the sucrose- and maltose-binding pockets in GR64a, we also performed alanine substitution mutagenesis studies followed by electrophysiological assays (Fig. 4, F and I, and fig. S2C). Among the eleven mutations that we tested, six on the aromatic residues that line the sugar-binding pocket—namely Phe¹³⁴, Phe¹³⁵, Tyr²³⁴, Trp²⁶⁰, Phe³³³, and Tyr³⁵³—as well as one on a conserved glutamate residue Glu¹⁹⁶ that forms hydrogen bonds with both sucrose and maltose (Fig. 4, E and H) abolished both sucrose- and maltose-induced currents (Fig. 4, F and I). Mutations on residues Tyr²⁰⁰ and Asn²⁵³, which form a CH- π interaction and a hydrogen bond with both sucrose and maltose, respectively (Fig. 4, E and H), did not affect sucrose or maltose activation (Fig. 4, F and I). Notably, the H197A and T257A mutants, although maintaining the maltose sensitivity, exhibited a complete loss in their sucrose sensitivity (Fig. 4, F and I). Because both His¹⁹⁷ and Thr²⁵⁷ form one hydrogen bond with maltose and sucrose (Fig. 4, E and H), disrupting the hydrogen bond likely affects the binding of sucrose but not maltose. Consistently, electrophysiological analyses showed that maltose (EC₅₀ = 10.2 \pm 3.1 mM) displays a higher affinity compared with sucrose (EC₅₀ = 21.9 \pm 7.1 mM) toward GR64a (Fig. 1, J and L). The differential sensitivities of H197A and T257A to sucrose versus maltose not only functionally confirm the disaccharide-binding pocket in GR64a but also provide insights into the sugar selectivity. Consistent results were seen when the mutant GR64 channels were analyzed using Ca²⁺ imaging assays (fig. S3, G to J).

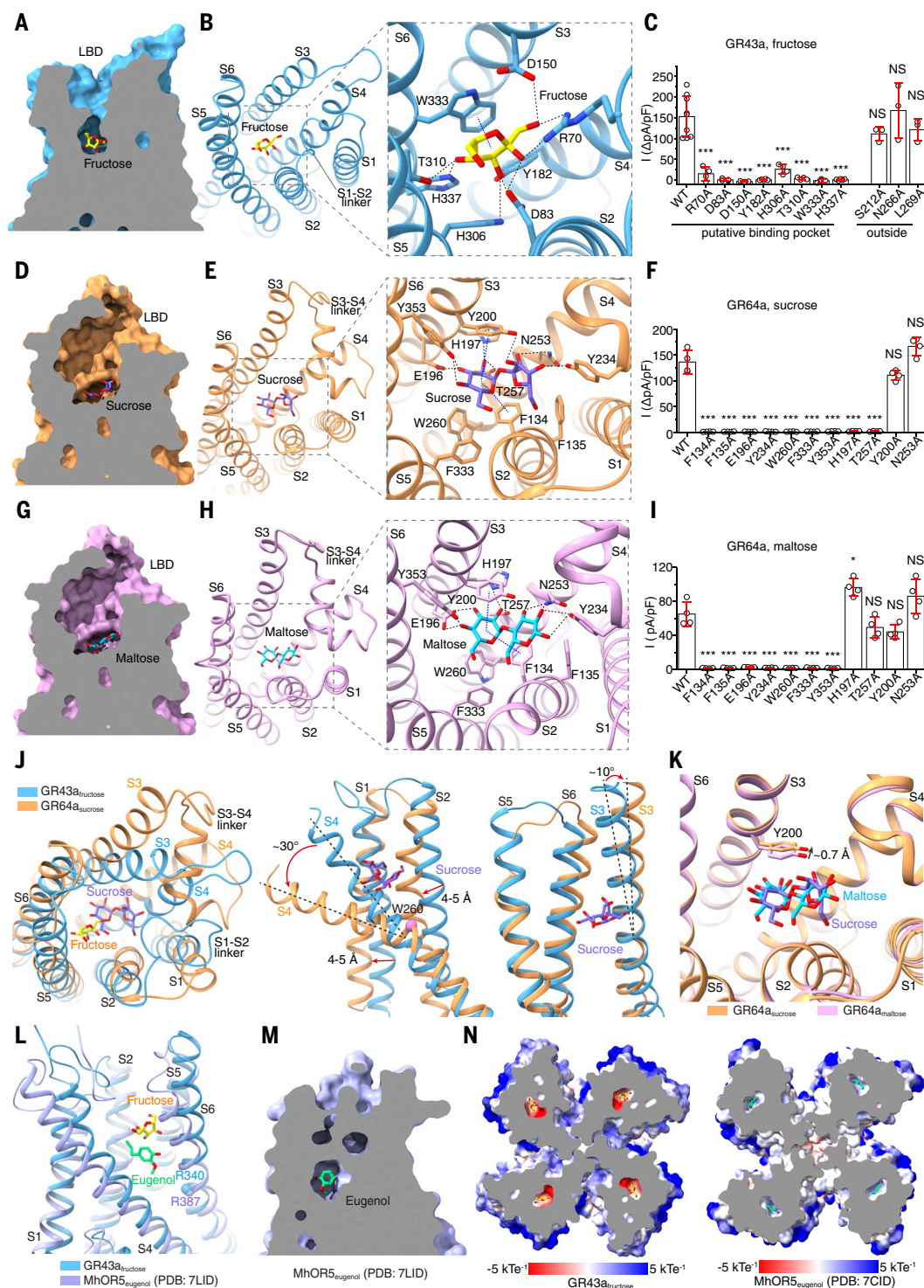


Fig. 4. Sugar-binding modes in GR43a and GR64a. (A) The fructose-binding pocket in GR43a LBD in the surface model in the cut-in side view. (B) Interactions between fructose and surrounding residues. The dashed lines in black indicate hydrogen bonds, and the dashed line in blue marks the CH- π interaction. (C) Density of fructose-evoked whole-cell currents ($\Delta A/pF$, measured at +120 mV) in HEK293FT cells transfected with WT or mutant GR43a. $n = 9, 4, 4, 3, 5, 4, 4, 4, 5, 3, 3$, and 3 independent experiments. (D) The sucrose-binding pocket in GR64a LBD in the surface model in the cut-in side view. (E) Interactions between sucrose and surrounding residues. (F) Density of sucrose-induced whole-cell currents ($\Delta A/pF$, measured at +120 mV) in HEK293FT cells

transfected with WT or mutant GR64a. $n = 4$ independent experiments. (G) The maltose-binding pocket in GR64a LBD in the surface model in the cut-in side view. (H) Interactions between maltose and surrounding residues. (I) Density of maltose-induced whole-cell currents ($\Delta A/pF$, measured at +120 mV) in HEK293FT cells transfected with WT or mutant GR64a. $n = 4$ independent experiments. (J) Superimposition of LBDs in GR43a_{fructose} (sky blue) and GR64a_{sucrose} (orange) in the top (left) and side views (middle and right). Compared with GR43a_{fructose}, conformational changes of S1 to S4 result in a large pocket in GR64a_{sucrose}. (K) Superimposition of sucrose- and maltose-bound states in GR64a. (L) Superimposition of LBDs in GR43a_{fructose} (sky blue) and MhOR5_{eugenol} (light slate)

blue) in side view. The conserved arginine residues in S6 are marked. **(M)** The eugenol-binding pocket in MhOR5 LBD in the surface model in the cut-in side view show that it is inaccessible from the extracellular side. **(N)** The electrostatic surface models show that fructose binds in a polar chemical environment in GR43a (left),

whereas eugenol binds in a hydrophobic environment in MhOR5 (right). In (C), (G), and (F), data are presented as means \pm SDs; two-tailed Student's *t* test was performed to compare the current density of cells expressing WT and each mutant of GRs. NS, not significant, $P > 0.05$; * $P < 0.05$; *** $P < 0.001$.

Molecular basis for the sugar selectivity

Comparisons of the sugar-binding modes in GR43a and GR64a reveal the principles for GRs' sugar selectivity. First, the size and shape of the ligand-binding pocket and the sugar molecule should match each other. In GR43a_{fructose}, the S2 to S6 helices as well as the S1-S2 linker build up a narrow pocket that may only stably accommodate the monosaccharide fructose with its five-membered furanose ring plane almost vertical to the membrane (Fig. 4, A and B). Five residues—namely Arg⁷⁰ in the S1-S2 linker, Thr⁸⁰ in S2, Trp¹⁵⁴ in S3, Phe³¹³ in S5, and Tyr³²⁶ in S6—are located at the mouth of the pocket and further constrain the entry of sugars (fig. S14A). Disaccharides, such as sucrose and maltose, are unlikely to enter this pocket, which otherwise would introduce steric hindrance with surrounding residues, as revealed by molecular docking (fig. S14, B, D, and E). Molecular docking also indicates that glucose binds in the pocket less stably than fructose (fig. S14, B and C), consistent with our electrophysiological data (Fig. 1, C and D). On the other hand, in GR64a, the long S3-S4 linker sitting on top of S4 pushes S1 to S4 away from the pocket center, resulting in a larger ligand-binding pocket (Fig. 4, D, E, G, and H). Compared with GR43a, the C-terminal part of S4 in GR64a bends by $\sim 30^\circ$ at the residue Trp²⁶⁰, along with a 4- to 5-Å shift of S1 and S2 and a $\sim 10^\circ$ tilting of the C-terminal part of S3. (Fig. 4J). Hence, the larger pocket allows GR64a to stably hold the disaccharides sucrose and maltose but not the smaller monosaccharides glucose and fructose owing to the lack of extra interactions (fig. S14, B and F to I), although they are both half parts of sucrose—i.e., the other half parts are essential for the stable binding for sucrose and maltose in the LBD of GR64a. Second, GRs recognize different sugars by specific interactions. Both GR43a and GR64a establish extensive hydrogen bonds and CH- π interactions with specific sugar molecules (Fig. 4, B, E, and H). Disrupting most of these interactions will eliminate the binding and activation effect of the sugars (Fig. 4, C, F, and I). Third, the structural plasticity of the ligand-binding pocket in a certain range allows one GR to sense more than one sugar. In GR64a, the glucose groups of sucrose and maltose do not align perfectly (Fig. 4K); as a consequence, the hydrogen bonds between the glucose groups and surrounding residues are not identical (Fig. 4, E and H). Compared with maltose, which has two glucose groups, sucrose pushes the side chain of Tyr²⁰⁰ away by ~ 0.7 Å with its fructose group (Fig. 4K). These differences in the binding modes of sucrose

and maltose in the LBD do not appear to substantially affect their activation on GR64a (Fig. 1, G and H). The structural plasticity of the ligand-binding pocket ensures that some GRs may be tuned to respond to more than one sugar (19–22).

Distinct perception modes of sweet tastants and odorants

Although GR43a and MhOR5 share similar overall architectures (fig. S10A), comparisons of ligand-bound structures of GR43a or GR64a and MhOR5 (50) reveal distinct perception modes of sweet tastants (nonvolatile and hydrophilic) and odorants (volatile and hydrophobic), both of which bind to specific pockets in LBDs. First, the odorant molecules eugenol and DEET in MhOR5 sit almost one-helical-turn deeper in the ligand-binding pocket compared with the sugar molecules in GR43a and GR64a (Fig. 4L and fig. S10B). Second, whereas the ligand-binding pocket in GR43a or GR64a generally opens to the extracellular side (Fig. 4, A, D, and G), it is closed by two layers of constriction predominately formed by hydrophobic residues in MhOR5 and therefore is inaccessible from the extracellular side (Fig. 4M and fig. S10, C and D). Third, sugar molecules bind to a polar chemical environment in GR43a and GR64a and form extensive hydrogen bonds and CH- π interactions with surrounding residues, whereas eugenol and DEET mainly form hydrophobic and/or π -stacking interactions in MhOR5 (50) (Fig. 4N and fig. S10E). These differences in perception modes of sweet tastants and odorants in GR43a and/or GR64a and MhOR5 are consistent with their different chemical properties. Sugars, such as fructose and sucrose, are nonvolatile, water-soluble, and polar molecules that tend to bind to a shallow and polar pocket from the extracellular side. By contrast, many odorants have a small polar surface area and low water solubility and therefore can bind to a deeper and hydrophobic pocket in LBDs presumably by diffusing into the hydrophobic membrane (50).

An open conformation of GR43a

Despite a clearly resolved fructose molecule in GR43a_{fructose}, the extracellular gate remains closed, as observed in GR43a_{apo} (Fig. 5, A and B). It is possible that some endogenous factors that support GR43a function in intact cells were missing in the protein samples for our structural studies. Because the I418A mutation resulted in a constitutively active channel that can be further activated by fructose (Fig. 3D), we solved the structures of the GR43a-I418A in the apo (GR43a_{I418A-apo}), fructose-bound

(GR43a_{I418A-fructose}), and fructose- and Ca²⁺-bound (GR43a_{I418A-fructose-Ca}) states at 2.8- to 3.1-Å resolutions (figs. S4 and S5). Notably, the fructose-bound GR43a_{I418A-fructose} structure exhibits several features that are different from those in the closed GR43a_{apo}. First, compared with that in GR43a_{apo}, the pore-lining S7b helix in GR43a_{I418A-fructose} bends by $\sim 10^\circ$ at Phe⁴⁰⁸, with its C-terminal part moving toward S2 in the same subunit (Fig. 5A). Second, along with the bending of S7b, the two layers of constrictions lined by hydrophobic residues Phe⁴²² and Ile⁴¹⁸ in GR43a_{apo} no longer exist in GR43a_{I418A-fructose}—the upper layer is replaced by the hydrophilic residue Gln⁴²¹, whereas the lower constriction disappears as a result of the outward motion of S7b as well as the substitution of Ile⁴¹⁸ by a smaller side chain residue Ala (Fig. 5, A and B). Third, the pore is dilated in GR43a_{I418A-fructose}, with a minimum radius of ~ 2 Å at the hydrophilic residue Gln⁴²¹ (Fig. 5B), large enough for the permeation of partially hydrated Na⁺ and K⁺. Thus, this GR43a_{I418A-fructose} structure is likely in an open state.

The fructose-bound GR43a_{I418A-fructose} exhibits similarities to the published eugenol-bound open-state MhOR5 (MhOR5_{eugenol}) (Fig. 5, A and C, and fig. S15) (50). In both structures, S7b bends at a hydrophobic residue (Phe⁴⁰⁸ in GR43a and Met⁴⁵⁴ in MhOR5) toward S2 in the same subunit, resulting in their respective constriction-lining hydrophobic residue (Phe⁴²² in GR43a and Val⁴⁶⁸ in MhOR5) moving away from the central pore axis and the conserved Gln residue (Gln⁴²¹ in GR43a and Gln⁴⁶⁷ in MhOR5) pointing to the central pore axis (Fig. 5, A and C, and fig. S15). These structural similarities between GR43a_{I418A-fructose} and MhOR5_{eugenol} suggest that the channel opening mechanisms might be conserved among GR and OR families.

Although no ion density was observed within the pore of MhOR5_{eugenol} (50), in the pore of GR43a_{I418A-fructose}, several density peaks were clearly resolved and modeled as water and Na⁺—the only major cation in the sample (Fig. 5D). Notably, one putative Na⁺ is located in the center of the ring formed by four Gln⁴²¹ side chains (Fig. 5D). The distance between the putative Na⁺ and the Gln⁴²¹ side chain is ~ 4 Å (Fig. 5D), which is too far for direct ion coordination. The oxygen atoms in the Gln⁴²¹ side chains likely stabilize the hydrated Na⁺ by acting as the second hydration shell. To probe the functional role of Gln⁴²¹, we generated two mutants, Q421N and Q421A. Although Q421A is nonfunctional, Q421N displayed a low constitutive activity with a complete loss of fructose sensitivity,

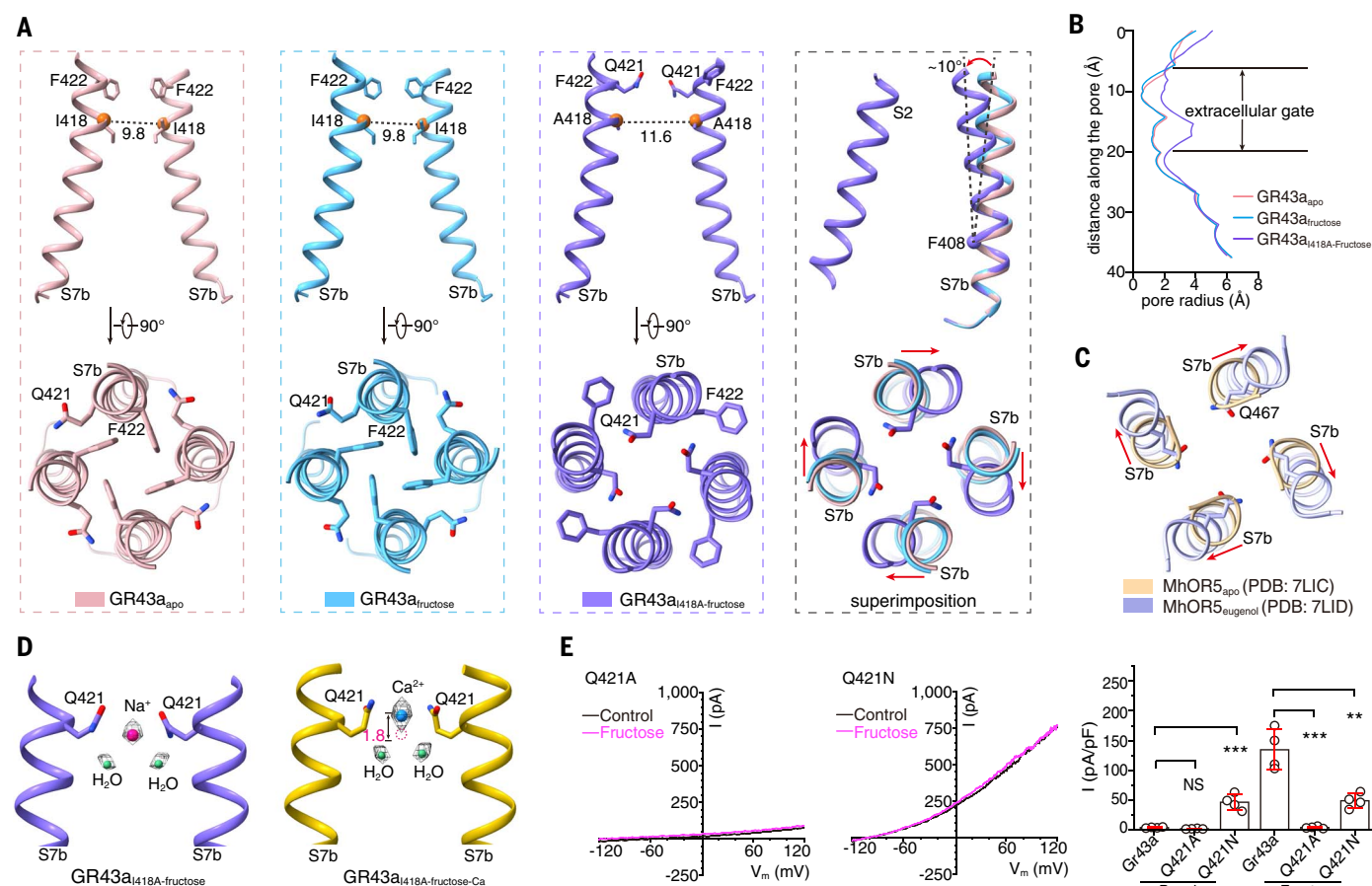


Fig. 5. The fructose-bound GR43a-I418A structure is in an open conformation. (A) Side and top views of the pore-lining S7b helices in three GR43a structures shown individually and superimposed. For clarity, in the side view, only two S7b helices are shown individually and only one S7b from three structures along with the intrasubunit S2 from GR43a_{I418A-fructose} is shown superimposed. Red arrows indicate the bending of S7b at Phe⁴⁰⁸. Key amino acid residues lining the pore are shown as sticks. Numbers above the dashed lines indicate distances (in angstroms) between diagonal Ca atoms of Ile⁴¹⁸ or Ala⁴¹⁸. (B) Pore radii of three GR43a structures along the central axis in the TMD calculated using the HOLE program. (C) Top view of the pore-lining S7b helices in the apo closed

which suggests an important role of Gln⁴²¹ in the channel activity (Fig. 5E). Moreover, in the pore of the fructose- and Ca²⁺-bound I418A mutant structure GR43a_{I418A-fructose-Ca}, one density peak, located $\sim 1.8 \text{ \AA}$ above the modeled Na⁺ in GR43a_{I418A-fructose}, was observed and putatively modeled as Ca²⁺ (Fig. 5D). These different ion densities in GR43a_{I418A-fructose-Ca} with Ca²⁺ and GR43a_{I418A-fructose} without Ca²⁺ not only cross-validate the ion-binding sites but also support the notion that Gln⁴²¹ is directly involved in the ion permeation through the central pore. A similar Gln residue in the selectivity filter was previously observed in TRPM channels, such as TRPM4 and TRPM8 (57–60).

The fructose activation mechanism of GR43a

Although the pore of GR43a_{fructose} remains closed, fructose induces conformational changes

in the LBD. To reveal the fructose activation mechanism, we first aligned the GR43a_{apo} and GR43a_{fructose} structures in the whole channel context (Fig. 6A). Upon the binding of fructose in the LBD, the C-terminal part of S5, the S5–S6 linker, and the N-terminal part of S6 move toward the pocket center by 1 to 3 Å, narrowing down the pocket entrance (Fig. 6B). The diagonal atom-to-atom distances of Thr⁸⁰–Tyr³²⁶ and Trp¹⁵⁴–Phe³¹³ decrease from 8.7 to 7.9 Å and from 7.8 to 6.2 Å, respectively (Fig. 6B and movie S2). These conformational changes are likely initiated by the establishment of a hydrogen bond between fructose and Thr³¹⁰ in S5 (Fig. 6B). However, the motion of the S5 C-terminal part does not induce a concerted conformational change of the S7b C-terminal part, and the extracellular gate of GR43a_{fructose} remains closed (Fig. 5B and Fig. 6C), probably

because of the decoupling of the LBD and PD in vitro. Such decoupling of the allosteric modulation domain and the PD was also observed in other ion channels in vitro, such as the voltage-gated potassium channel KCNQs in the absence of PIP₂ (62–64).

To reveal the LBD–PD coupling mechanism, we next aligned the GR43a_{fructose} and GR43a_{I418A-fructose} structures (Fig. 6D). At the LBD–PD interface, the main chains of amino acid residues in the C-terminal part of S5 remain almost unchanged (Fig. 6E). By contrast, side chains of three aromatic residues in S5—namely Tyr³¹², Phe³¹³, and Phe³¹⁵—undergo an anticlockwise rotation from GR43a_{fructose} to GR43a_{I418A-fructose} when viewed from the extracellular side along with a so-called flip-up of the Phe³¹⁵ side chain (Fig. 6E). Whereas the Phe³¹³ side chain points to the LBD center and its rotation likely

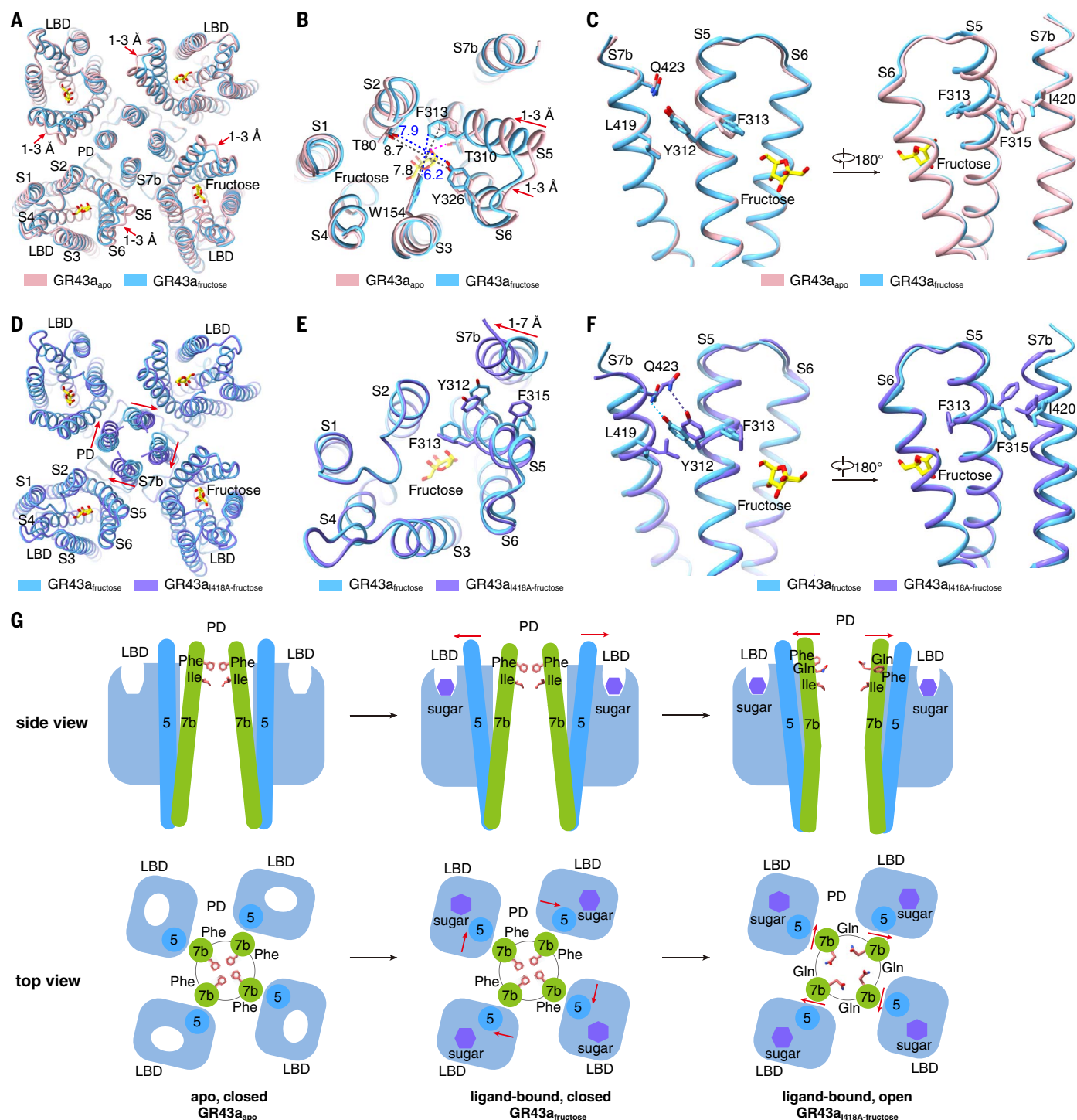


Fig. 6. The structural mechanism for the activation of GR43a by fructose.

(A) Structural alignment of GR43a_{apo} and GR43a_{fructose} in the top view. Red arrows indicate the motions of the C-terminal part of S5, the S5-S6 linker, and the N-terminal part of S6. (B) A zoom-in view of the closing up of the ligand-binding pocket in the presence of fructose. Dashed lines in black and blue indicate diagonal atom-to-atom distances (in angstroms) before and after fructose binding, respectively. The local conformational change of the LBD is likely initiated by the hydrogen bond (red dashed line) of fructose and Thr³¹⁰ in S5. (C) Side views of interactions between S5 and S7b before and after the fructose binding. Conformational change in S5 does not induce concerted

conformational change in S7b. (D) Structural alignment of GR43a_{fructose} and GR43a_{I418A-fructose} in the top view. Red arrows indicate the motions of the C-terminal part of S5, the S5-S6 linker, and the N-terminal part of S6. (E) A zoom-in view of the conformational differences in S5 and S7b between GR43a_{fructose} and GR43a_{I418A-fructose}. (F) Side views of interactions between S5 and S7b in GR43a_{fructose} and GR43a_{I418A-fructose}. Conformational changes of Tyr³¹² and Phe³¹⁵ in S5 accompany the bending of S7b in GR43a_{I418A-fructose}. (G) The proposed fructose activation model of GR43a. Fructose binds to LBD to induce a rotation of S5, which in turn causes the bending of S7b, along with the hydrophobic Phe moving away and the hydrophilic Gln pointing toward to the pore center, resulting in the opening of the channel.

provides space for Tyr³¹², both Tyr³¹² and Phe³¹⁵ directly interact with amino acid residues in the pore-lining S7b (Fig. 6E). Specifically, Phe³¹⁵ forms hydrophobic interactions with Ile⁴²⁰, and Tyr³¹² forms a hydrogen bond with Gln⁴²³ and hydrophobic interactions with Leu⁴¹⁹ (Fig. 6F). Thus, through these direct interactions, the conformational changes of Tyr³¹² and Phe³¹⁵ may further induce the bending of S7b toward the intrasubunit S2, leading to an ultimate opening of the channel (movie S3).

Taken together, structures of GR43a_{apo}, GR43a_{fructose}, and GR43a_{I418A-fructose} represent ligand-free closed, ligand-bound closed (decoupled), and ligand-bound open conformations of GR43a, respectively. Overall, these structures provide snapshots to the channel opening processes upon fructose binding to the LBD in GR43a (Fig. 6G and movies S2 to S4).

Discussion

The accurate detection of nutrients is crucial for insects to regulate their feeding behavior, growth, and metabolism. Previous bioinformatic, genetic, and physiological studies of *Drosophila* GRs have identified a series of sweet taste receptors (17–27). In this work, we have performed comprehensive functional and structural analyses of the sweet taste receptors by focusing on GR43a and GR64a as model systems. Our structures show that GR43a and GR64a assemble into tetrameric ligand-gated ion channels, with the PD formed by four S7b helices and the LBD formed by S1 to S6 in each subunit. In GR43a, fructose binds to LBD to induce local conformational changes, which are then transferred to the PD to cause channel opening. The sugar selectivity of different GRs largely depends on the size and shape of the ligand-binding pockets in LBDs. Although previous in vivo studies have suggested that some GRs likely form heteromeric oligomers to respond to different sugars and other tastants (22, 26, 29, 33, 34), the homotetramer structures of GR43a and GR64a lay a foundation for structure-function analysis of insect GRs.

We use the I418A mutant to capture the open conformation of GR43a. Several lines of evidence support that the GR43a_{I418A-fructose} structure represents an open conformation of GR43a. First, structures of the I418A mutant in the apo and fructose-bound states largely agree with its electrophysiological activities. I418A displayed a high basal activity and can be further activated by fructose (Fig. 3D). Consistently, in the structure GR43a_{I418A-apo}, S7b already bends toward S2, with Gln⁴²¹ pointing to the pore center, similar to that in GR43a_{I418A-fructose} (fig. S16). However, careful examination of the S7b C-terminal part shows that the gate in GR43a_{I418A-apo} opens not as widely as that in GR43a_{I418A-fructose} (fig. S16). Thus, the GR43a_{I418A-apo} structure is likely in a partially open state, and fructose may induce further opening of the gate, as seen in GR43a_{I418A-fructose}.

Second, a recent study on BmGR-9 showed that mutation of Ile⁴⁴⁰ (equivalent to Ile⁴¹⁸ in GR43a) to alanine resulted in similar constitutive activity of the channel (48). Third, the PD conformation of GR43a_{I418A-fructose} displays a high similarity to that of MhOR5^{eugenol}, which suggests a common gating mechanism conserved for both GR and OR families (Fig. 5, A to C, and fig. S15). Fourth, although Ile⁴¹⁸ is a pore-lining residue that forms the second layer of constriction in the closed state (GR43a_{apo}), an elimination of this constriction in GR43a_{I418A-fructose} is not simply a result of the replacement of Ile⁴¹⁸ by the smaller side chain residue Ala but may be primarily caused by the outward motion of S7b, as revealed by the enlarged diagonal distances from C α atoms of Ile⁴¹⁸ (9.8 Å) to those of Ala⁴¹⁸ (11.6 Å) in two structures (Fig. 5A). We hypothesize that the I418A mutation might have reduced the activation energy required for the closed-to-open conformational transition, possibly by weakening the intersubunit hydrophobic interactions; in the presence of fructose, a fully open conformation of GR43a can be captured. Although we were unable to capture the open conformation of fructose-bound WT GR43a in the current study, it is not uncommon that an ion channel can be function-wise in the open state in cells but structure-wise in the closed state in vitro (65, 66). Nevertheless, the fructose-bound GR43a_{I418A-fructose} structure has provided useful structural information for deciphering the sugar activation mechanism of GR43a.

In GR64a, neither maltose nor sucrose causes major conformational changes because all the structures of GR64a_{apo}, GR64a_{maltose}, and GR64a_{sucrose} are essentially in the same conformation (fig. S17A). In these structures, constrictions in the PD are formed by the hydrophobic residue Val⁴³⁸ (equivalent to Ile⁴¹⁸ in GR43a) and the hydrophilic residue Gln⁴⁴¹ (equivalent to Gln⁴²¹ in GR43a), with diagonal atom-to-atom distances of 6.1 and 4.9 Å, respectively (fig. S17, B to D). Although the hydrophilic Gln⁴⁴¹ adopts a similar conformation to that of the equivalent Gln residues in open-state GR43a_{I418A-fructose} and MhOR5^{eugenol}, the hydrophobic constriction lined by Val⁴³⁸ indicates that these GR64a structures are still in a closed state (fig. S17, B and C). To capture an open conformation of GR64a, besides Val⁴³⁸, we also mutated adjacent residues located close to the extracellular gate, such as Gln⁴⁴¹ and Phe⁴⁴², but none of them resulted in any constitutive channel activity. Hence, thermodynamic properties may vary among the related but different GR proteins—e.g., GR43a and GR64a.

Compared with the human sweet taste receptor, *Drosophila* sweet taste receptors display several different features in their molecular mechanisms. First, human taste buds sense sweet taste mainly by the heterodimeric G protein-coupled receptor TAS1R2-TAS1R3 (67–70), which then activates the intracellular inositol

3-phosphate signaling pathway and finally causes the release of the neurotransmitter adenosine 5'-triphosphate (ATP) via CALHM channels (71, 72). By contrast, our in vitro functional and structural analyses reveal that *Drosophila* sweet taste receptors GR43a and GR64a are ionotropic receptors that themselves form sugar-activated ion channels, providing a simple pathway for sweet taste sensation. Second, although both TAS1R2-TAS1R3 and GRs contain seven transmembrane helices, their topologies, structures, and their sugar recognition modes are different. In TAS1R2-TAS1R3, sugar molecules mainly bind to the extracellular Venus flytrap (VFT) domain of TAS1R2 (73, 74). The sugar-bound GR43a and GR64a structures show that both the monosaccharide and disaccharides bind to the LBD of the TMD through extensive hydrogen bonds and CH- π interactions, representing a new sugar recognition mode. Third, it is interesting that *Drosophila* has at least nine GRs that are sensitive to different sugars, whereas humans sense different sweet tastants by only one heterodimeric receptor. In *Drosophila*, functional expression of multiple sugar receptors may confer an advantage not only in detecting but also in discriminating a broad range of sugar chemicals in fruit, leading to more precise physiological and behavioral responses for adaption to diverse environments. Understanding the sugar binding and activation mechanisms of different GRs may guide the development of strategies to tune the physiology and behavior of insects as well as to control pests (75, 76).

Materials and methods

Protein expression and purification

The full-length *D. melanogaster* GR43a and GR64a genes containing a Strep tag II were cloned into the pEZT-BM vector (77). GR43a and GR64a were both heterologously expressed in human embryonic kidney HEK293S GnT1[−] suspension cells (ATCC, no. CRL-3022) using the BacMam system (Thermo Fisher Scientific). The P2 baculovirus generated in Sf9 cells (ATCC, no. CRL-1711) following standard protocol was used to transfect HEK293S GnT1[−] cells at a ratio of 1:10 (virus: HEK293S, v/v) when the cell density was around 3.5×10^6 cells/ml. To boost protein expression, 10 mM sodium butyrate was added to the cell culture. After incubation for 48 hours, cells were harvested, flash-frozen in liquid nitrogen, and stored at -80°C until needed.

Cells were resuspended and lysed by sonication in buffer A (20 mM HEPES, pH 7.4, 150 mM NaCl) supplemented with a protease inhibitor cocktail [2 $\mu\text{g/ml}$ deoxyribonuclease (DNase) I, 0.5 $\mu\text{g/ml}$ pepstatin, 2 $\mu\text{g/ml}$ leupeptin, 1 $\mu\text{g/ml}$ aprotinin, and 1 mM phenylmethylsulfonyl fluoride (PMSF)]. GR43a protein was extracted with 1.5% (w/v) n-dodecyl- β -D-maltopyranoside (DDM) (Anatrace) and 0.3% (w/v) cholesteryl hemisuccinate (CHS) (Anatrace) by gentle agitation for

3 hours at 4°C. After extraction, the insoluble cell fragment was removed by centrifugation at $48,000 \times g$ for 50 min at 4°C. Then the supernatant was incubated gently with Strep-Tactin Sepharose resin 4FF (Smart-Lifesciences) at 4°C. After 1.5 hours, the resin was collected on a gravity column (BBI Life Sciences) and washed with buffer B (buffer A + 0.05% DDM + 0.01% CHS) for 4 column volumes (CVs) and then with buffer C [buffer A + 0.03% (w/v) glyco-diosgenin (GDN) (Anatrace)] for 16 CVs. The protein sample was eluted with 10 mM *d*-Desthiobiotin (Sigma-Aldrich) in buffer C and further purified by size-exclusion chromatography on the Superose 6 10/300 GL column (GE Healthcare) (fig. S4A). The peak fraction of GR43a was collected and concentrated to 14 mg/ml for cryo-EM analysis. The GR64a protein was purified following the same procedure except that 1.5% (w/v) lauryl maltose neopentyl glycol (LMNG) (Anatrace) was used to extract the protein from the cell membrane. The peak fraction of GR64a in size-exclusion chromatography was collected and concentrated to 16 mg/ml for cryo-EM analysis (fig. S6A).

Cryo-EM sample preparation and data acquisition

The cryo-EM grids were prepared by applying 3 μ l of GR43a/GR64a protein sample to a glow-discharged holey carbon grid (Quantifoil Au R1.2/1.3, 300 mesh) and blotted for 4.5 s under 100% humidity at 4°C before being plunged into liquid ethane using a Mark IV Vitrobot (FEI). For the samples of GR43a or GR64a in the presence of three sugars, the concentrated GRs proteins were mixed with fructose (Sigma-Aldrich), maltose (Sigma-Aldrich), or sucrose (Sigma-Aldrich) to a final concentration of 10 mM. For the sample of the GR43a I418A mutant in the presence of Ca^{2+} , 10 mM Ca^{2+} was added in the concentrated sample. After incubation at 4°C for 45 min, the mixture samples were used for cryo-EM sample preparation.

The cryo-EM data were collected at Center of Cryo-Electron Microscopy at Zhejiang University. Micrographs were acquired on the Titan Krios microscope (FEI) operating at 300 kV equipped with the Selectris energy filter (Thermo Fisher Scientific) and Gatan Falcon 4 detector. EPU software was used for automated data collection according to standard procedures. A calibrated magnification of $\times 130,000$ was used for imaging, yielding a pixel size of 0.93 Å on images. The defocus range was set from -0.8 to $-1.5 \mu\text{m}$. Each micrograph was dose-fractionated to 40 frames under a dose rate of 7.49 e^- per pixel per second, with a total exposure time of 6 s, resulting in a total dose of about 52 $\text{e}^- \text{Å}^{-2}$.

Image processing

Motion correction and CTF parameters estimation were performed with the MotionCorr2 (78) and the GCTF (79) programs, respectively. All

following image processing steps were carried out with RELION 3.1 (80) (fig. S4C and fig. S6C). For GR43a_{apo}, 2850 micrographs were collected, and 1,516,194 particles were auto-picked and extracted with a binning factor of 3 for three-dimensional (3D) classification. Three rounds of 3D classification were performed using the initial model generated by RELION as a reference. After 3D classification, selected particles were re-extracted to the pixel size of 0.93 Å for 3D refinement with *C4* symmetry and Bayesian polishing. The final 3D reconstruction of GR43a_{apo} from 263,979 particles yielded an EM map with a resolution of 2.6 Å.

For the fructose-bound GR43a structure GR43a_{fructose}, 2979 micrographs were collected, and 1,579,102 particles were auto-picked and extracted with a binning factor of 3 for 2D classification. Three rounds of 3D classification were performed using the initial model of GR43a_{apo} as a reference. After 3D classification, selected particles were re-extracted to the pixel size of 0.93 Å for 3D refinement with *C4* symmetry and Bayesian polishing. The final 3D reconstruction from 240,297 particles yielded an EM map with a resolution of 2.5 Å.

For the apo/fructose-bound/fructose- Ca^{2+} -bound structures of the GR43a I418A mutant (GR43a_{I418A-apo}/GR43a_{I418A-fructose}/GR43a_{I418A-fructose-Ca}), 3460/3569/3504 micrographs were collected, and 1,823,299/1,735,579/1,914,274 particles were auto-picked and extracted with a binning factor of 3 for 2D classification. Two rounds of 3D classification were performed using the initial model of GR43a_{apo} as a reference. After 3D classification, selected particles were re-extracted to the pixel size of 0.93 Å for 3D refinement with *C4* symmetry and Bayesian polishing. The final 3D reconstruction of GR43a_{I418A-apo}/GR43a_{I418A-fructose}/GR43a_{I418A-fructose-Ca} from 200,231/158,079/84,051 particles yielded an EM map with a resolution of 2.8/2.8/3.1 Å.

For GR64a_{apo}, 2831 micrographs were collected, and 1,526,976 particles were auto-picked and extracted with a binning factor of 3 for 2D classification. Two rounds of 3D classification were performed using the initial model of GR43a_{apo} as a reference. After 3D classification, selected particles were re-extracted to the pixel size of 0.93 Å for 3D refinement with *C4* symmetry and Bayesian polishing. The final 3D reconstruction of GR64a_{apo} from 372,952 particles yielded an EM map with a resolution of 2.5 Å.

For the sugar-bound GR64a structures GR64a_{sucrose}/GR64a_{maltose}, 3454/3267 micrographs were collected, and 1,903,295/1,804,025 particles were auto-picked and extracted with a binning factor of 3 for 2D classification. Two rounds of 3D classification were performed using the initial model of GR64a_{apo} as a reference. After 3D classification, selected particles were re-extracted to the pixel size of 0.93 Å for 3D refinement with *C4* symmetry and Bayesian polishing. The final

3D reconstruction of GR64a_{sucrose}/GR64a_{maltose} from 632,430/529,197 particles yielded an EM map with a resolution of 2.5/2.6 Å.

The resolution was estimated by applying a soft mask around the protein density and the gold-standard Fourier shell correlation (FSC) = 0.143 criterion (fig. S4E and fig. S6E). Local resolution maps were calculated with RELION 3.1 (80) (fig. S4D and fig. S6D).

To verify the *C4* symmetry of GR43a and GR64a structures, we also used the *C1* symmetry to perform 3D reconstruction of these GR43a and GR64a structures, which all largely maintain the *C4* symmetry, as shown by the superimposition of *C1* and *C4* maps (fig. S9).

Model building, refinement, and validation

De novo atomic models were built in Coot (81) based on the 2.6- and 2.5-Å resolution maps of GR43a_{apo} and GR64a_{apo}. The GR43a_{apo} and GR64a_{apo} atomic models were built using the GR43a and GR64a structures predicted by AlphaFold II as starting templates. Structure models were refined in PHENIX (82) against cryo-EM maps using real-space refinement, with secondary structure restraints and noncrystallography symmetry applied. The models of GR43a_{fructose}, GR43a_{I418A-apo}, GR43a_{I418A-fructose}, and GR43a_{I418A-fructose-Ca} were built using the model of GR43a_{apo} as a template, and the models of GR64a_{sucrose} and GR64a_{maltose} were built using the model of GR64a_{apo} as a template. Structure models were validated with MolProbity (83) (fig. S4E, fig. S6E, and table S1). The van der Waals radii of the pore were calculated using HOLE (84) (Fig. 3, A and F; Fig. 5B; and fig. S17C). Structural figures were prepared in PyMOL (The PyMOL Molecular Graphics System, version 1.8, Schrödinger, LLC.), Chimera X (85), or Coot (81).

Whole-cell patch-clamp electrophysiology

HEK293FT cells were purchased from Thermo Fisher (R70007) and cultured in a high glucose DMEM (Gibco) medium with 10% fetal bovine serum (FBS) (VivaCell). All cells were used at low passages with occasional authentication for mycoplasma contamination using MycoAlert™ Mycoplasma Detection Kit (LT07-218, Lonza). Full-length GR43a and GR64a genes were cloned to the pIRES2-EGFP vector, which were then transfected to HEK293FT cells with Lipofectamine 3000 (Invitrogen) according to the manufacturing instruction. Site-directed mutagenesis was performed using either a QuikChange II Site-Directed Mutagenesis Kit (200,523, Agilent) or a Gibson Assembly Cloning Kit (E5510S, New England Biolabs). All constructs were confirmed by DNA sequencing.

Ionic currents were recorded in the whole-cell configuration under voltage-clamp using an Axopatch 200B amplifier equipped with a Digidata 1440A digitizer (Molecular Devices). A ramp protocol (-120 mV to $+120$ mV, 400-ms duration, holding at 0 mV) or a step protocol

(−120 mV to +120 mV, 200-ms duration, with a 20-mV increment) was used to record the currents. To study the time course of channel activation, the recordings were performed using the ramp protocol at 2-s intervals. Unless otherwise stated, the pipette (cytosolic) solution contained (in millimolar): 135 Cs-methanesulfonic acid (MSA), 10 TEA-OH, and 20 HEPES (pH was adjusted to 7.2 with CsOH). Note that MSA[−] is often used to substitute physiological anions such as Cl[−] in the recording solutions for the electrophysiological studies of cation channels. The pipette solution was supplemented with essential Cl[−] (2 mM) needed to stably conduct electricity through Ag/AgCl electrode. The bath solution contained sugar with indicated concentration (280 mM for a standard bath solution) and mannitol buffered with 20 mM HEPES (pH was adjusted to 7.2), bringing the final osmolarity to ~300 mOsm. Note that the osmotic coefficient is >1 for sugars, ~0.93 for NaCl/KCl, and 0.86 for CaCl₂. The bath solutions were applied via a fast perfusion system that allowed us to achieve complete solution exchange within a few seconds. An agar bridge filled with 3M KCl was used for the reference electrode. Glass electrodes were pulled with a resistance of 2 to 4 megaohm. Data were collected using a Clampex 10.7 software (Molecular Devices). All experiments were performed at room temperature (22° to 25°C), and all data were analyzed with Clampfit 10.7 (Molecular Devices) and Origin pro 2021 (OriginLab).

The permeability of GR43a and GR64a for cations (Na⁺, K⁺, or Ca²⁺) relative to Cs⁺ was estimated based on the Goldman-Hodgkin-Katz current equations (Eq. 1 for monovalents and Eq. 2 for Ca²⁺) (86) and the measured E_{rev} under bi-ionic conditions

$$\frac{P_X}{P_{Cs}} = \frac{[Cs^+]_i}{[X^+]_e} e^{(FV/RT)} \quad (1)$$

$$\frac{P_{Ca}}{P_{Cs}} = \frac{[Cs^+]_i}{4[Ca^{2+}]_e} e^{(FV/RT)} \left(e^{(FV/RT)} + 1 \right) \quad (2)$$

where R , T , F , and V are the gas constant, absolute temperature, Faraday's constant, and the reversal potential, respectively. The activity coefficients are assumed to be 1 for monovalent ions and 0.75 for Ca²⁺. The liquid junction potentials were measured and corrected as described (87). The reversal potential (E_{rev}) was determined based on the traces recorded using a ramp protocol (−120 mV to +120 mV, 400 ms, holding at 0 mV) in response to bath solutions containing (in millimolar): 130 Na-MSA/130 K-MSA/100 CaCl₂ and 20 HEPES, supplemented with 30 fructose (for GR43a) or 30 sucrose (for GR64a).

To provide an independent functional verification of our electrophysiological data from

HEK293FT cells, we also performed electrophysiological recordings of both GR43a and GR64a channels in two nonhuman cell lines: Chinese Hamster Ovary (CHO) (RRID, no. CVCL_U429) and COS1 monkey cell (ATCC, no. CRL-1650) lines.

Fura-2 Ca²⁺ imaging

HEK293FT cells were loaded with Fura-2 (3 μM) and Pluronic-F127 (3 μM) in the culture medium at 37°C for 30 min. Before imaging, cells were bathed in the Tyrode's solution containing (in millimolar): 145 NaCl, 5 KCl, 2 or 10 CaCl₂, 1 MgCl₂, and 20 HEPES, pH adjusted to 7.4. Imaging solutions containing (in millimolar): 280 Fructose, 10 CaCl₂, 5 KCl, and 20 HEPES, pH 7.4 were used to study GR43a; imaging solutions containing (in millimolar): 280 sucrose/maltose, 2 CaCl₂, 5 KCl, and 20 HEPES, pH 7.4 were used to study GR64a. Fura-2 fluorescent ratio (F340/F380) was recorded at two different wavelengths (340 and 380 nm) using a Sutter Lambda 721 imaging system and quantified with Fiji (ImageJ).

Molecular docking

Molecular docking was performed by watvina, which is developed based on Autodock vina (88) and qvina2 (89). The scoring function is composed of van der Waals, hydrogen bond, and pseudo electrostatic interaction, which are calculated by Lenard Jones 12-6, Morse potential, and sigmoid function, respectively. The parameters of van der Waals interactions were derived from the CHARMM36m force field. For the hydrogen bond, the Morse potential was set to −1.0 if the distance between polar hydrogen and acceptor was shorter than the optimal distance. A sigmoid potential was used to approximate the electrostatic interaction which accounts for the polar-polar repulsion or nonpolar-nonpolar attraction interaction. Genetic algorithm (GA) was used for the global conformation searching. Broyden-Fletcher-Goldfarb-Shanno (BFGS) algorithm or Stochastic Steepest Descent (SSD) algorithm was used for local optimization. The initial 3D conformation of fructose, glucose, maltose, and sucrose for docking to GR43a protein were built by Avogadro and minimized using MMFF94s force field and steepest descent algorithm (90). The initial conformation of glucose and fructose for docking to GR64a were derived from the sucrose in the GR64a_{sucrose} structure, after GA global searching and SSD local searching. The protonation state of protein was determined by UCSF Chimera considering optimization of hydrogen bond network. Each docking was repeated at eight times. The conformations with top intermolecule scores were analyzed. All the structures were converted to pdbqt format by rdkit2pdbqt.py script, which is improved on the atom-typing, rotatable bond definition, and ROOT atoms selection based on the open drug discovery

toolkit (91). The watvina program and rdkit2pdbqt.py script are accessible on Github (<https://github.com/biocheming/watvina>).

All-atom MD simulation

To validate the sugar-binding modes in GR43a and GR64a, monomer models representing sugar-bound GR43a and GR64a were constructed using docking structures. Additionally, to explore the potential involvement of lipids in GR43a, an atomistic model was generated based on the cryo-EM structure of GR43a_{apo}. These models were then incorporated into a flat POPC lipid bilayer and immersed in a cubic water box containing 0.15 M NaCl. Two distinct periodic rectangular boxes were used for the monomer and tetramer models, with approximate dimensions of 7 × 7 × 11 nm and 11.6 × 11.6 × 10.6 nm, resulting in ~50,000 and 148,000 atoms for each model, respectively. The TM region in the lipid bilayer was aligned using the OPM (Orientations of Proteins in Membranes) webserver (92). The systems were built with the CHARMM-GUI webserver (93) and underwent an energy minimization step using the steepest descent algorithm, followed by a six-step equilibration during which position constraints in the systems were gradually removed. Finally, production runs in semi-isothermal-isobaric (NPT) conditions were performed using the CHARMM36m force field (CHARMM36m for protein and lipids, and TIP3P for water) (94). The force field parameters for the sugars were obtained from CGenFF (95). In the MD simulations, the temperature was kept constant at 310 K using a Nosé-Hoover thermostat with a 1-ps coupling constant, and the pressure at 1.0 bar using the Parrinello-Rahman barostat with a 5-ps time coupling constant. A switch function starting at 1.0 nm was used to apply a cut-off of 1.2 nm for the van der Waals interactions. The cut-off for the short-range electrostatic interactions was also 1.2 nm, and the long-range electrostatic interactions were calculated by means of the particle mesh Ewald decomposition algorithm with a 0.12-nm mesh spacing. A reciprocal grid of 100 × 100 × 96 cells was used with fourth-order B-spline interpolation. The adiabatic bias molecular dynamics (ABMD) method (96) was used to add a ratchet-and-pawl-like potential with a force constant of 0.01 kJ/mol/nm² along the coordination number between the POPC tails and the sidechains of Phe⁴⁰⁸, Ala⁴⁰⁹, Tyr⁴¹⁵, Ala⁴¹³, and Leu⁴¹⁶ to push the lipid tail away from the lipid-binding sites around Tyr⁴¹⁵. Two independent 50-ns ABMD simulations were performed for the tetramer model, and four independent 500-ns simulation trajectories were conducted for the monomer models.

The coarse-grained (CG) model of GR43a was constructed using the Martini 3.0 force field (97) and prepared using the martinize.py program. The CG model was subsequently embedded in a

POPC lipid bilayer with dimensions of $11.7 \times 11.7 \times 11.0$ nm using the INSANE protocol (98). The protein structure was restrained using the elastic network model, with a force constant of 500 kJ/mol/nm^2 . The systems were solvated using a CG Martini water model and neutralized by adding NaCl at a concentration of 0.15 M. The CG system was minimized for 5000 steps with the steepest descent method and subsequently equilibrated by following the standard CHARMMGUI equilibrium protocol. Finally, each production run was performed in the semi-isotropic NPT ensemble using a time step of 20 fs. Two independent CG MD simulations, $\sim 60 \mu\text{s}$ each, were performed. The temperature of the system was kept at 310 K with the velocity rescaling thermostat. The pressure was kept at 1 bar using the Parrinello-Rahman barostat with a compressibility of $3 \times 10^{-4} \text{ bar}^{-1}$ and a coupling constant of 12 ps.

All simulations were performed using a GPU-accelerated version of Gromacs 2021.4 or 2022.5 (99). Trajectories were analyzed using Gromacs gmx tools and PLUMED 2.8.2 (100).

REFERENCES AND NOTES

- J. Chandrasekhar, M. A. Hoon, N. J. Ryba, C. S. Zuker, The receptors and cells for mammalian taste. *Nature* **444**, 288–294 (2006). doi: [10.1038/nature05401](#); pmid: [17108952](#)
- D. A. Yarmolinsky, C. S. Zuker, N. J. Ryba, Common sense about taste: From mammals to insects. *Cell* **139**, 234–244 (2009). doi: [10.1016/j.cell.2009.10.001](#); pmid: [19837029](#)
- E. R. Liman, Y. V. Zhang, C. Montell, Peripheral coding of taste. *Neuron* **81**, 984–1000 (2014). doi: [10.1016/j.neuron.2014.02.022](#); pmid: [24607224](#)
- C. Montell, A taste of the *Drosophila* gustatory receptors. *Curr. Opin. Neurobiol.* **19**, 345–353 (2009). doi: [10.1016/j.conb.2009.07.001](#); pmid: [19660932](#)
- Y. D. Chen, A. Dahanukar, Recent advances in the genetic basis of taste detection in *Drosophila*. *Cell. Mol. Life Sci.* **77**, 1087–1101 (2020). doi: [10.1007/s00018-019-03320-0](#); pmid: [31598735](#)
- E. G. Freeman, A. Dahanukar, Molecular neurobiology of *Drosophila* taste. *Curr. Opin. Neurobiol.* **34**, 140–148 (2015). doi: [10.1016/j.conb.2015.06.001](#); pmid: [26102453](#)
- B. Shrestha, Y. Lee, Molecular sensors in the taste system of *Drosophila*. *Genes Genomics* **45**, 693–707 (2023). doi: [10.1007/s13258-023-01370-0](#); pmid: [36828965](#)
- K. Scott, Gustatory processing in *Drosophila melanogaster*. *Annu. Rev. Entomol.* **63**, 15–30 (2018). doi: [10.1146/annurev-ento-020117-043331](#); pmid: [29324046](#)
- R. M. Joseph, J. R. Carlson, *Drosophila* chemoreceptors: A molecular interface between the chemical world and the brain. *Trends Genet.* **31**, 683–695 (2015). doi: [10.1016/j.tig.2015.09.005](#); pmid: [26477743](#)
- P. J. Clyne, C. G. Warr, J. R. Carlson, Candidate taste receptors in *Drosophila*. *Science* **287**, 1830–1834 (2000). doi: [10.1126/science.287.5459.1830](#); pmid: [10710312](#)
- K. Scott *et al.*, A chemosensory gene family encoding candidate gustatory and olfactory receptors in *Drosophila*. *Cell* **104**, 661–673 (2001). doi: [10.1016/S0092-8674\(01\)00263-X](#); pmid: [11257221](#)
- L. Dunipace, S. Meister, C. McNealy, H. Amrein, Spatially restricted expression of candidate taste receptors in the *Drosophila* gustatory system. *Curr. Biol.* **11**, 822–835 (2001). doi: [10.1016/S0960-9822\(01\)00258-5](#); pmid: [11516643](#)
- H. M. Robertson, C. G. Warr, J. R. Carlson, Molecular evolution of the insect chemoreceptor gene superfamily in *Drosophila melanogaster*. *Proc. Natl. Acad. Sci. U.S.A.* **100**, 14537–14542 (2003). doi: [10.1073/pnas.2335847100](#); pmid: [14608037](#)
- M. Murakami, H. Kijima, Transduction ion channels directly gated by sugars on the insect taste cell. *J. Gen. Physiol.* **115**, 455–466 (2000). doi: [10.1085/jgp.115.4.455](#); pmid: [10736312](#)
- K. Touhara, L. B. Vosshall, Sensing odorants and pheromones with chemosensory receptors. *Annu. Rev. Physiol.* **71**, 307–332 (2009). doi: [10.1146/annurev.physiol.010908.163209](#); pmid: [19575682](#)
- K. Sato, K. Tanaka, K. Touhara, Sugar-regulated cation channel formed by an insect gustatory receptor. *Proc. Natl. Acad. Sci. U.S.A.* **108**, 11680–11685 (2011). doi: [10.1073/pnas.1019622108](#); pmid: [21709218](#)
- A. Dahanukar, K. Foster, W. M. van der Goes van Naters, J. R. Carlson, A *Gr* receptor is required for response to the sugar trehalose in taste neurons of *Drosophila*. *Nat. Neurosci.* **4**, 1182–1186 (2001). doi: [10.1038/nn765](#); pmid: [11704765](#)
- K. Ueno *et al.*, Trehalose sensitivity in *Drosophila* correlates with mutations in and expression of the gustatory receptor gene *Gr5a*. *Curr. Biol.* **11**, 1451–1455 (2001). doi: [10.1016/S0960-9822\(01\)00450-X](#); pmid: [11566105](#)
- A. Dahanukar, Y. T. Lei, J. Y. Kwon, J. R. Carlson, Two *Gr* genes underlie sugar reception in *Drosophila*. *Neuron* **56**, 503–516 (2007). doi: [10.1016/j.neuron.2007.10.024](#); pmid: [17988633](#)
- Y. Jiao, S. J. Moon, C. Montell, A *Drosophila* gustatory receptor required for the responses to sucrose, glucose, and maltose identified by mRNA tagging. *Proc. Natl. Acad. Sci. U.S.A.* **104**, 14110–14115 (2007). doi: [10.1073/pnas.0702421104](#); pmid: [17715294](#)
- J. Slone, J. Daniels, H. Amrein, Sugar receptors in *Drosophila*. *Curr. Biol.* **17**, 1809–1816 (2007). doi: [10.1016/j.cub.2007.09.027](#); pmid: [17919910](#)
- Y. Jiao, S. J. Moon, X. Wang, Q. Ren, C. Montell, Gr64f is required in combination with other gustatory receptors for sugar detection in *Drosophila*. *Curr. Biol.* **18**, 1797–1801 (2008). doi: [10.1016/j.cub.2008.10.009](#); pmid: [19026541](#)
- T. Miyamoto, J. Slone, X. Song, H. Amrein, A fructose receptor functions as a nutrient sensor in the *Drosophila* brain. *Cell* **151**, 1113–1125 (2012). doi: [10.1016/j.cell.2012.10.024](#); pmid: [23178127](#)
- D. Mishra *et al.*, The molecular basis of sugar sensing in *Drosophila* larvae. *Curr. Biol.* **23**, 1466–1471 (2013). doi: [10.1016/j.cub.2013.06.028](#); pmid: [23850280](#)
- E. G. Freeman, Z. Wisotsky, A. Dahanukar, Detection of sweet tastants by a conserved group of insect gustatory receptors. *Proc. Natl. Acad. Sci. U.S.A.* **111**, 1598–1603 (2014). doi: [10.1073/pnas.1311724111](#); pmid: [24474785](#)
- A. Yavuz, C. Jagge, J. Slone, H. Amrein, A genetic tool kit for cellular and behavioral analyses of insect sugar receptors. *Fly* **8**, 189–196 (2014). doi: [10.1080/19336934.2015.1050569](#); pmid: [25984594](#)
- S. Fujii *et al.*, *Drosophila* sugar receptors in sweet taste perception, olfaction, and internal nutrient sensing. *Curr. Biol.* **25**, 621–627 (2015). doi: [10.1016/j.cub.2014.12.058](#); pmid: [25702577](#)
- S. J. Moon, M. Kötting, Y. Jiao, H. Xu, C. Montell, A taste receptor required for the caffeine response *in vivo*. *Curr. Biol.* **16**, 1812–1817 (2006). doi: [10.1016/j.cub.2006.07.024](#); pmid: [16979558](#)
- Y. Lee, S. J. Moon, C. Montell, Multiple gustatory receptors required for the caffeine response in *Drosophila*. *Proc. Natl. Acad. Sci. U.S.A.* **106**, 4495–4500 (2009). doi: [10.1073/pnas.0811744106](#); pmid: [19246397](#)
- S. J. Moon, Y. Lee, Y. Jiao, C. Montell, A *Drosophila* gustatory receptor essential for aversive taste and inhibiting male-to-male courtship. *Curr. Biol.* **19**, 1623–1627 (2009). doi: [10.1016/j.cub.2009.07.061](#); pmid: [19765987](#)
- L. A. Weiss, A. Dahanukar, J. Y. Kwon, D. Banerjee, J. R. Carlson, The molecular and cellular basis of bitter taste in *Drosophila*. *Neuron* **69**, 258–272 (2011). doi: [10.1016/j.neuron.2011.01.001](#); pmid: [21262465](#)
- H. K. M. Dweck, J. R. Carlson, Molecular logic and evolution of bitter taste in *Drosophila*. *Curr. Biol.* **30**, 17–30.e3 (2020). doi: [10.1016/j.cub.2019.11.005](#); pmid: [31839451](#)
- W. D. Jones, P. Cayirlioglu, I. G. Kadow, L. B. Vosshall, Two chemosensory receptors together mediate carbon dioxide detection in *Drosophila*. *Nature* **445**, 86–90 (2007). doi: [10.1038/nature05466](#); pmid: [17167414](#)
- J. Y. Kwon, A. Dahanukar, L. A. Weiss, J. R. Carlson, The molecular basis of CO₂ reception in *Drosophila*. *Proc. Natl. Acad. Sci. U.S.A.* **104**, 3574–3578 (2007). doi: [10.1073/pnas.0700079104](#); pmid: [17360684](#)
- S. Bray, H. Amrein, A putative *Drosophila* pheromone receptor expressed in male-specific taste neurons is required for efficient courtship. *Neuron* **39**, 1019–1029 (2003). doi: [10.1016/S0896-6273\(03\)00542-7](#); pmid: [12971900](#)
- T. Miyamoto, H. Amrein, Suppression of male courtship by a *Drosophila* pheromone receptor. *Nat. Neurosci.* **11**, 874–876 (2008). doi: [10.1038/nn.2161](#); pmid: [18641642](#)
- L. Ni *et al.*, A gustatory receptor paralogue controls rapid warmth avoidance in *Drosophila*. *Nature* **500**, 580–584 (2013). doi: [10.1038/nature12390](#); pmid: [23925112](#)
- Y. Xiang *et al.*, Light-avoidance-mediating photoreceptors tile the *Drosophila* larval body wall. *Nature* **468**, 921–926 (2010). doi: [10.1038/nature09576](#); pmid: [21068723](#)
- J. Gong *et al.*, The *C. elegans* taste receptor homolog LITE-1 is a photoreceptor. *Cell* **167**, 1252–1263.e10 (2016). doi: [10.1016/j.cell.2016.10.053](#); pmid: [27863243](#)
- Y. Lee, S. H. Kim, C. Montell, Avoiding DEET through insect gustatory receptors. *Neuron* **67**, 555–561 (2010). doi: [10.1016/j.neuron.2010.07.006](#); pmid: [20797533](#)
- H. Guo, K. Kunwar, D. Smith, Multiple channels of DEET repellency in *Drosophila*. *Pest Manag. Sci.* **76**, 880–887 (2020). doi: [10.1002/ps.5592](#); pmid: [21649190](#)
- E. J. Dennis, O. V. Goldman, L. B. Vosshall, *Aedes aegypti* mosquitoes use their legs to sense DEET on contact. *Curr. Biol.* **29**, 1551–1556.e5 (2019). doi: [10.1016/j.cub.2019.04.004](#); pmid: [31031114](#)
- H. Amrein, N. Thorne, Gustatory perception and behavior in *Drosophila melanogaster*. *Curr. Biol.* **15**, R673–R684 (2005). doi: [10.1016/j.cub.2005.08.021](#); pmid: [16139201](#)
- T. Miyamoto, G. Wright, H. Amrein, Nutrient sensors. *Curr. Biol.* **23**, R369–R373 (2013). doi: [10.1016/j.cub.2013.04.002](#); pmid: [23660359](#)
- N. Yapici, R. Cohn, C. Schusterreiter, V. Ruta, L. B. Vosshall, A taste circuit that regulates ingestion by integrating food and hunger signals. *Cell* **165**, 715–729 (2016). doi: [10.1016/j.cell.2016.02.061](#); pmid: [27040496](#)
- T. Miyamoto, H. Amrein, Diverse roles for the *Drosophila* fructose sensor Gr43a. *Fly* **8**, 19–25 (2014). doi: [10.4161/fly.27241](#); pmid: [24406333](#)
- Q. P. Wang *et al.*, Sucralose promotes food intake through NPY and a neuronal fasting response. *Cell Metab.* **24**, 75–90 (2016). doi: [10.1016/j.cmet.2016.06.010](#); pmid: [27411010](#)
- S. Moringa *et al.*, Structural model for ligand binding and channel opening of an insect gustatory receptor. *J. Biol. Chem.* **298**, 102573 (2022). doi: [10.1016/j.jbc.2022.102573](#); pmid: [36209821](#)
- K. Palczewski *et al.*, Crystal structure of rhodopsin: A G protein-coupled receptor. *Science* **289**, 739–745 (2000). doi: [10.1126/science.289.5480.739](#); pmid: [10926528](#)
- J. del Marmol, M. A. Yedlin, V. Ruta, The structural basis of odorant recognition in insect olfactory receptors. *Nature* **597**, 126–131 (2021). doi: [10.1038/s41586-021-03794-8](#); pmid: [34349260](#)
- H. M. Robertson, The insect chemoreceptor superfamily is ancient in animals. *Chem. Senses* **40**, 609–614 (2015). doi: [10.1093/chemse/bjv046](#); pmid: [26354932](#)
- K. Saotome *et al.*, Structure of the mechanically activated ion channel Piezo1. *Nature* **554**, 481–486 (2018). doi: [10.1038/nature25453](#); pmid: [29261642](#)
- Q. Zhao *et al.*, Structure and mechanogating mechanism of the Piezo1 channel. *Nature* **554**, 487–492 (2018). doi: [10.1038/nature25743](#); pmid: [29469092](#)
- H. M. Berman *et al.*, The Protein Data Bank. *Nucleic Acids Res.* **28**, 235–242 (2000). doi: [10.1093/nar/28.1.235](#); pmid: [10592235](#)
- L. L. Kiessling, R. C. Diehl, CH- π interactions in glycan recognition. *ACS Chem. Biol.* **16**, 1884–1893 (2021). doi: [10.1021/acscchembio.1c00413](#); pmid: [34615357](#)
- S. Faham *et al.*, The crystal structure of a sodium galactose transporter reveals mechanistic insights into Na⁺/sugar symport. *Science* **321**, 810–814 (2008). doi: [10.1126/science.1160406](#); pmid: [18599740](#)
- J. Guo *et al.*, Structures of the calcium-activated, non-selective cation channel TRPM4. *Nature* **552**, 205–209 (2017). doi: [10.1038/nature24997](#); pmid: [29211714](#)
- H. E. Aultzen *et al.*, Structure of the human TRPM4 ion channel in a lipid nanodisc. *Science* **359**, 228–232 (2018). doi: [10.1126/science.aar4510](#); pmid: [29217581](#)
- P. A. Winkler, Y. Huang, W. Sun, J. Du, W. Lü, Electron cryo-microscopy structure of a human TRPM4 channel. *Nature* **552**, 200–204 (2017). doi: [10.1038/nature24674](#); pmid: [29211723](#)
- J. Duan *et al.*, Structure of full-length human TRPM4. *Proc. Natl. Acad. Sci. U.S.A.* **115**, 2377–2382 (2018). doi: [10.1073/pnas.1722038115](#); pmid: [29463718](#)
- C. Zhao *et al.*, Structures of a mammalian TRPM8 in closed state. *Nat. Commun.* **13**, 3113 (2022). doi: [10.1038/s41467-022-30919-y](#); pmid: [35662242](#)
- J. Sun, R. MacKinnon, Cryo-EM structure of a KCNQ1/CaM complex reveals insights into congenital long QT syndrome.

- Cell* **169**, 1042–1050.e9 (2017). doi: [10.1016/j.cell.2017.05.019](https://doi.org/10.1016/j.cell.2017.05.019); pmid: [28575668](https://pubmed.ncbi.nlm.nih.gov/28575668/)
63. X. Li *et al.*, Molecular basis for ligand activation of the human KCNQ2 channel. *Cell Res.* **31**, 52–61 (2021). doi: [10.1038/s41422-020-00410-8](https://doi.org/10.1038/s41422-020-00410-8); pmid: [32884139](https://pubmed.ncbi.nlm.nih.gov/32884139/)
 64. D. Ma *et al.*, Structural mechanisms for the activation of human cardiac KCNQ1 channel by electro-mechanical coupling enhancers. *Proc. Natl. Acad. Sci. U.S.A.* **119**, e2207067119 (2022). doi: [10.1073/pnas.2207067119](https://doi.org/10.1073/pnas.2207067119); pmid: [36763058](https://pubmed.ncbi.nlm.nih.gov/36763058/)
 65. N. Gan *et al.*, Structural mechanism of allosteric activation of TRPML1 by PI(3,5)P₂ and rapamycin. *Proc. Natl. Acad. Sci. U.S.A.* **119**, e2120404119 (2022). doi: [10.1073/pnas.2120404119](https://doi.org/10.1073/pnas.2120404119); pmid: [35131932](https://pubmed.ncbi.nlm.nih.gov/35131932/)
 66. J. Payandeh, T. Scheuer, N. Zheng, W. A. Catterall, The crystal structure of a voltage-gated sodium channel. *Nature* **475**, 353–358 (2011). doi: [10.1038/nature10238](https://doi.org/10.1038/nature10238); pmid: [21743477](https://pubmed.ncbi.nlm.nih.gov/21743477/)
 67. M. A. Hoon *et al.*, Putative mammalian taste receptors: A class of taste-specific GPCRs with distinct topographic selectivity. *Cell* **96**, 541–551 (1999). doi: [10.1016/S0092-8674\(00\)80658-3](https://doi.org/10.1016/S0092-8674(00)80658-3); pmid: [10052456](https://pubmed.ncbi.nlm.nih.gov/10052456/)
 68. M. Max *et al.*, *Tas1r3*, encoding a new candidate taste receptor, is allelic to the sweet responsiveness locus *Sac*. *Nat. Genet.* **28**, 58–63 (2001). doi: [10.1038/ng0501-58](https://doi.org/10.1038/ng0501-58); pmid: [11326277](https://pubmed.ncbi.nlm.nih.gov/11326277/)
 69. J. P. Montmayeur, S. D. Liberles, H. Matsunami, L. B. Buck, A candidate taste receptor gene near a sweet taste locus. *Nat. Neurosci.* **4**, 492–498 (2001). doi: [10.1038/87440](https://doi.org/10.1038/87440); pmid: [11319557](https://pubmed.ncbi.nlm.nih.gov/11319557/)
 70. G. Nelson *et al.*, Mammalian sweet taste receptors. *Cell* **106**, 381–390 (2001). doi: [10.1016/S0092-8674\(01\)00451-2](https://doi.org/10.1016/S0092-8674(01)00451-2); pmid: [11509186](https://pubmed.ncbi.nlm.nih.gov/11509186/)
 71. A. Taruno *et al.*, CALHM1 ion channel mediates purinergic neurotransmission of sweet, bitter and umami tastes. *Nature* **495**, 223–226 (2013). doi: [10.1038/nature11906](https://doi.org/10.1038/nature11906); pmid: [23467090](https://pubmed.ncbi.nlm.nih.gov/23467090/)
 72. Z. Ma *et al.*, CALHM3 is essential for rapid ion channel-mediated purinergic neurotransmission of GPCR-mediated tastes. *Neuron* **98**, 547–561.e10 (2018). doi: [10.1016/j.neuron.2018.03.043](https://doi.org/10.1016/j.neuron.2018.03.043); pmid: [29681531](https://pubmed.ncbi.nlm.nih.gov/29681531/)
 73. H. Xu *et al.*, Different functional roles of TIR subunits in the heteromeric taste receptors. *Proc. Natl. Acad. Sci. U.S.A.* **101**, 14258–14263 (2004). doi: [10.1073/pnas.0404384101](https://doi.org/10.1073/pnas.0404384101); pmid: [15353592](https://pubmed.ncbi.nlm.nih.gov/15353592/)
 74. N. Nuemket *et al.*, Structural basis for perception of diverse chemical substances by T1r taste receptors. *Nat. Commun.* **8**, 15530 (2017). doi: [10.1038/ncomms15530](https://doi.org/10.1038/ncomms15530); pmid: [28534491](https://pubmed.ncbi.nlm.nih.gov/28534491/)
 75. W. van der Goes van Naters, J. R. Carlson, Insects as chemosensors of humans and crops. *Nature* **444**, 302–307 (2006). doi: [10.1038/nature05403](https://doi.org/10.1038/nature05403); pmid: [17108954](https://pubmed.ncbi.nlm.nih.gov/17108954/)
 76. L. S. Baik, J. R. Carlson, The mosquito taste system and disease control. *Proc. Natl. Acad. Sci. U.S.A.* **117**, 32848–32856 (2020). doi: [10.1073/pnas.2013076117](https://doi.org/10.1073/pnas.2013076117); pmid: [33372129](https://pubmed.ncbi.nlm.nih.gov/33372129/)
 77. C. L. Morales-Perez, C. M. Novello, R. E. Hibbs, Manipulation of subunit stoichiometry in heteromeric membrane proteins. *Structure* **24**, 797–805 (2016). doi: [10.1016/j.str.2016.03.004](https://doi.org/10.1016/j.str.2016.03.004); pmid: [27041595](https://pubmed.ncbi.nlm.nih.gov/27041595/)
 78. S. Q. Zheng *et al.*, MotionCor2: Anisotropic correction of beam-induced motion for improved cryo-electron microscopy. *Nat. Methods* **14**, 331–332 (2017). doi: [10.1038/nmeth.4193](https://doi.org/10.1038/nmeth.4193); pmid: [28250466](https://pubmed.ncbi.nlm.nih.gov/28250466/)
 79. K. Zhang, Gctf: Real-time CTF determination and correction. *J. Struct. Biol.* **193**, 1–12 (2016). doi: [10.1016/j.jsb.2015.11.003](https://doi.org/10.1016/j.jsb.2015.11.003); pmid: [26592709](https://pubmed.ncbi.nlm.nih.gov/26592709/)
 80. J. Zivanov *et al.*, New tools for automated high-resolution cryo-EM structure determination in RELION-3. *eLife* **7**, e42166 (2018). doi: [10.7554/eLife.42166](https://doi.org/10.7554/eLife.42166); pmid: [30412051](https://pubmed.ncbi.nlm.nih.gov/30412051/)
 81. P. Emsley, B. Lohkamp, W. G. Scott, K. Cowtan, Features and development of Coot. *Acta Cryst.* **D66**, 486–501 (2010). doi: [10.1107/S0907444910007493](https://doi.org/10.1107/S0907444910007493); pmid: [20383002](https://pubmed.ncbi.nlm.nih.gov/20383002/)
 82. P. D. Adams *et al.*, PHENIX: A comprehensive Python-based system for macromolecular structure solution. *Acta Cryst.* **D66**, 213–221 (2010). doi: [10.1107/S0907444909052925](https://doi.org/10.1107/S0907444909052925); pmid: [20124702](https://pubmed.ncbi.nlm.nih.gov/20124702/)
 83. V. B. Chen *et al.*, MolProbity: All-atom structure validation for macromolecular crystallography. *Acta Cryst.* **D66**, 12–21 (2010). doi: [10.1107/S0907444909042073](https://doi.org/10.1107/S0907444909042073); pmid: [20057044](https://pubmed.ncbi.nlm.nih.gov/20057044/)
 84. O. S. Smart, J. G. Neduvellil, X. Wang, B. A. Wallace, M. S. P. Sansom, HOLE: A program for the analysis of the pore dimensions of ion channel structural models. *J. Mol. Graph.* **14**, 354–360 (1996). doi: [10.1016/S0263-7855\(97\)00009-X](https://doi.org/10.1016/S0263-7855(97)00009-X); pmid: [9195488](https://pubmed.ncbi.nlm.nih.gov/9195488/)
 85. E. F. Pettersen *et al.*, UCSF ChimeraX: Structure visualization for researchers, educators, and developers. *Protein Sci.* **30**, 70–82 (2021). doi: [10.1002/pro.3943](https://doi.org/10.1002/pro.3943); pmid: [32881101](https://pubmed.ncbi.nlm.nih.gov/32881101/)
 86. C. A. Lewis, Ion-concentration dependence of the reversal potential and the single channel conductance of ion channels at the frog neuromuscular junction. *J. Physiol.* **286**, 417–445 (1979). doi: [10.1113/jphysiol.1979.sp012629](https://doi.org/10.1113/jphysiol.1979.sp012629); pmid: [312319](https://pubmed.ncbi.nlm.nih.gov/312319)
 87. E. Neher, Correction for liquid junction potentials in patch clamp experiments. *Methods Enzymol.* **207**, 123–131 (1992). doi: [10.1016/0076-6879\(92\)07008-C](https://doi.org/10.1016/0076-6879(92)07008-C); pmid: [1528115](https://pubmed.ncbi.nlm.nih.gov/1528115)
 88. O. Trott, A. J. Olson, AutoDock Vina: Improving the speed and accuracy of docking with a new scoring function, efficient optimization, and multithreading. *J. Comput. Chem.* **31**, 455–461 (2010). doi: [10.1002/jcc.21334](https://doi.org/10.1002/jcc.21334); pmid: [19499576](https://pubmed.ncbi.nlm.nih.gov/19499576/)
 89. A. Alhossary, S. D. Handoko, Y. Mu, C. K. Kwok, Fast, accurate, and reliable molecular docking with QuickVina 2. *Bioinformatics* **31**, 2214–2216 (2015). doi: [10.1093/bioinformatics/btv082](https://doi.org/10.1093/bioinformatics/btv082); pmid: [25717194](https://pubmed.ncbi.nlm.nih.gov/25717194/)
 90. M. D. Hanwell *et al.*, Avogadro: An advanced semantic chemical editor, visualization, and analysis platform. *J. Cheminform.* **4**, 17 (2012). doi: [10.1186/1758-2946-4-17](https://doi.org/10.1186/1758-2946-4-17); pmid: [22889332](https://pubmed.ncbi.nlm.nih.gov/22889332/)
 91. M. Wójcikowski, P. Zielenkiewicz, P. Siedlecki, Open Drug Discovery Toolkit (ODDT): A new open-source player in the drug discovery field. *J. Cheminform.* **7**, 26 (2015). doi: [10.1186/s13321-015-0078-2](https://doi.org/10.1186/s13321-015-0078-2); pmid: [26101548](https://pubmed.ncbi.nlm.nih.gov/26101548/)
 92. M. A. Lomize, I. D. Pogozheva, H. Joo, H. I. Mosberg, A. L. Lomize, OPM database and PPM web server: Resources for positioning of proteins in membranes. *Nucleic Acids Res.* **40**, D370–D376 (2012). doi: [10.1093/nar/gkr703](https://doi.org/10.1093/nar/gkr703); pmid: [21890895](https://pubmed.ncbi.nlm.nih.gov/21890895/)
 93. S. Jo, T. Kim, V. G. Iyer, W. Im, CHARMM-GUI: A web-based graphical user interface for CHARMM. *J. Comput. Chem.* **29**, 1859–1865 (2008). doi: [10.1002/jcc.20945](https://doi.org/10.1002/jcc.20945); pmid: [18351591](https://pubmed.ncbi.nlm.nih.gov/18351591/)
 94. J. Huang *et al.*, CHARMM36m: An improved force field for folded and intrinsically disordered proteins. *Nat. Methods* **14**, 71–73 (2017). doi: [10.1038/nmeth.4067](https://doi.org/10.1038/nmeth.4067); pmid: [27819658](https://pubmed.ncbi.nlm.nih.gov/27819658/)
 95. K. Vanommeslaeghe *et al.*, CHARMM general force field: A force field for drug-like molecules compatible with the CHARMM all-atom additive biological force fields. *J. Comput. Chem.* **31**, 671–690 (2010). doi: [10.1002/jcc.21367](https://doi.org/10.1002/jcc.21367); pmid: [19575467](https://pubmed.ncbi.nlm.nih.gov/19575467/)
 96. Y. Wang, E. Papaleo, K. Lindorff-Larsen, Mapping transiently formed and sparsely populated conformations on a complex energy landscape. *eLife* **5**, e17505 (2016). doi: [10.7554/eLife.17505](https://doi.org/10.7554/eLife.17505); pmid: [27552057](https://pubmed.ncbi.nlm.nih.gov/27552057/)
 97. P. C. T. Souza *et al.*, Martini 3: A general purpose force field for coarse-grained molecular dynamics. *Nat. Methods* **18**, 382–388 (2021). doi: [10.1038/s41592-021-01098-3](https://doi.org/10.1038/s41592-021-01098-3); pmid: [33782607](https://pubmed.ncbi.nlm.nih.gov/33782607/)
 98. T. A. Wassenaar, H. I. Ingólfsson, R. A. Böckmann, D. P. Tieleman, S. J. Marrink, Computational Lipidomics with insane: A Versatile Tool for Generating Custom Membranes for Molecular Simulations. *J. Chem. Theory Comput.* **11**, 2144–2155 (2015). doi: [10.1021/acs.jctc.5b00209](https://doi.org/10.1021/acs.jctc.5b00209); pmid: [26574417](https://pubmed.ncbi.nlm.nih.gov/26574417/)
 99. M. J. Abraham *et al.*, GROMACS: High performance molecular simulations through multi-level parallelism from laptops to supercomputers. *SoftwareX* **1**, 19–25 (2015). doi: [10.1016/j.softx.2015.06.001](https://doi.org/10.1016/j.softx.2015.06.001)
 100. PLUMED consortium, Promoting transparency and reproducibility in enhanced molecular simulations. *Nat. Methods* **16**, 670–673 (2019). doi: [10.1038/s41592-019-0506-8](https://doi.org/10.1038/s41592-019-0506-8); pmid: [31363226](https://pubmed.ncbi.nlm.nih.gov/31363226/)

ACKNOWLEDGMENTS

Single-particle cryo-EM data were collected at the Center of Cryo-Electron Microscopy at Zhejiang University. We thank X. Zhang for his support in cryo-EM facility access and data acquisition.

Funding: This work was supported in part by grants from the Ministry of Science and Technology of China (2020YFA0908501 to J.G. and 2020YFA0908500 to S.Y.), the National Key Research and Development Program of China (2022YFE0210100 to H.X. and 2021YFF1200404 to Y.W.), the New Cornerstone Investigator Program (to H.X.), the National Science Foundation of China (32371204 to J.G. and 32371300 to Y.W.), Zhejiang Provincial Natural Science Foundation (LR19C050002 to J.G. and LZ24C050003 to Y.W.), and the Fundamental Research Funds for the Central Universities (to J.G., N.S., and Y.W.). J.G. and H.X. are also supported by the MOE Frontier Science Center for Brain Science and Brain-machine Integration, Zhejiang University. M.F. is supported by the CAS Center for Excellence in Molecular Plant Sciences/Institute of Plant Physiology and Ecology and the CAS Pioneer Hundred Talents Program. **Author contributions:** J.G., H.X., M.F., and N.S. conceived and supervised the project. D.M., N.S., S.C., and R.W. performed sample preparation, data acquisition, and structure determination. M.H., X.Y., Q.L., and W.C. performed electrophysiology and Ca²⁺ imaging assays. F.Y., Y.W., and X.X. conducted MD simulations and molecular dockings. J.G., H.X., M.F., N.S., S.Y., and W.Y. performed data analysis. All authors participated in the data analysis and manuscript preparation. **Competing interests:** H.X. is the scientific cofounder and a partial owner of Lysoway Therapeutics Inc. (Boston, MA). The authors declare no other competing interests. **Data and materials availability:** Structure coordinates and cryo-EM maps have been deposited in the Protein Data Bank and the Electron Microscopy Data Bank under accession numbers 8JM9 and EMD-36410 for GR43a_{apo}, 8JMA and EMD-36411 for GR43a_{fructose}, 8X82 and EMD-38133 for GR43a_{418A-3apo}, 8X83 and EMD-38134 for GR43a_{418A-fructose}, 8X84 and EMD-38135 for GR43a_{418A-fructose-Ca}, 8JME and EMD-36417 for GR64a_{apo}, 8JMH and EMD-36421 for GR64a_{sucrose}, and 8JMI and EMD-36422 for GR64a_{maltose}. All other data are presented in the main text or supplementary materials. **License information:** Copyright © 2024 the authors, some rights reserved; exclusive licensee American Association for the Advancement of Science. No claim to original US government works. <https://www.science.org/about/science-licenses-journal-article-reuse>

SUPPLEMENTARY MATERIALS

science.org/doi/10.1126/science.adj2609

Figs. S1 to S17

Table S1

MDAR Reproducibility Checklist

Movies S1 to S4

Submitted 16 June 2023; resubmitted 28 November 2023

Accepted 17 January 2024

Published online 1 February 2024

10.1126/science.adj2609